1 # Assessment of the impact of spatial heterogeneity on

2 # microwave satellite soil moisture periodic error

3 **Fangni Lei[a,b], Wade T. Crow[a], Huanfeng Shen[b], Chun-Hsu Su[c], Thomas R. H. Holmes[d],**

4 **Robert M. Parinussa[e], Guojie Wang[f]**

5

6 [a]*USDA ARS Hydrology and Remote Sensing Laboratory, Beltsville, MD 20705, USA*

7 [b]*School of Resource and Environmental Sciences, Wuhan University, Wuhan, Hubei 430072, China*

8 [c]*Department of Infrastructure Engineering, University of Melbourne, Parkville, Victoria 3010, Australia*

9 [d]*NASA GSFC Hydrological Sciences Laboratory, Greenbelt, MD 20771, USA*

10 [e]*Transmissivity B.V./VanderSat B.V., Space Technology Business Park, Huygenstraat 34, Noordwijk 2201*

11 *DK, The Netherlands*

12 [f]*School of Geography and Remote Sensing, Nanjing University of Information Science and Technology,*

13 *Nanjing, Jiangsu 210044, China*

14

15

16   **Abstract:**

17   An accurate temporal and spatial characterization of errors is required for the efficient processing,

18   evaluation, and assimilation of remotely-sensed surface soil moisture retrievals. However,

19   empirical evidence exists that passive microwave soil moisture retrievals are prone to periodic

20   artifacts which may complicate their application in data assimilation systems (which commonly

21   treat observational errors as being temporally white). In this paper, the link between such

22   temporally-periodic errors and spatial land surface heterogeneity is examined. Both the synthetic

23   experiment and site-specified cases reveal that, when combined with strong spatial heterogeneity,

24   temporal periodicity in satellite sampling patterns (associated with exact repeat intervals of the

25   polar-orbiting satellites) can lead to spurious high frequency spectral peaks in soil moisture

26   retrievals. In addition, the global distribution of the most prominent and consistent 8-day spectral

27   peak in the Advanced Microwave Scanning Radiometer – Earth Observing System soil moisture

28   retrievals is revealed via a peak detection method. Three spatial heterogeneity indicators – based

29   on microwave brightness temperature, land cover types, and long-term averaged vegetation index

30   – are proposed to characterize the degree to which the variability of land surface is capable of

31   inducing periodic error into satellite-based soil moisture retrievals. Regions demonstrating 8-day

32   periodic errors are generally consistent with those exhibiting relatively higher heterogeneity

33   indicators. This implies a causal relationship between spatial land surface heterogeneity and

34   temporal periodic error in remotely-sensed surface soil moisture retrievals.

35

I. Introduction

Within the past two decades, extensive efforts have been aimed at enhancing remote estimation of surface soil moisture. Currently, several global space-borne soil moisture products are available from a series of satellite-based passive and/or active microwave sensors. The accurate characterization of global satellite-derived soil moisture products is crucial for multiple hydrological (Srivastava et al., 2013; Wagner et al., 2007a), meteorological (Koster et al., 2004; Seneviratne et al., 2010), agricultural (Bolten et al., 2010; Engman et al., 1991; Lakhankar et al., 2009a), and natural hazardous (Lacava et al., 2005) applications. Especially in hydrological data assimilation community, the inclusion of satellite-based soil moisture observations has drawn great attention for the purposes of catchment rainfall-runoff (Alvarez-Garreton et al., 2014; Crow et al., 2009; Komma et al., 2008) and both continental (Crow and Zhan, 2007; Walker and Houser, 2004) and global-scale (Reichle and Koster, 2005; Reichle et al., 2004; 2007) land surface modeling.

Recently, Su et al. (2013a; 2015) presented a spectrally-based approach for evaluating satellite-derived soil moisture retrievals, which builds upon a semi-empirical water balance model and operates in the frequency domain. Based on this approach, they identified periodic error components in passive microwave retrieved soil moisture Level 3 (gridded) retrieval products acquired from both the Advanced Microwave Scanning Radiometer – Earth Observing System (AMSR-E) and the Soil Moisture and Ocean Salinity (SMOS) missions, suggesting the need to consider the presence of temporally-periodic errors when using and/or evaluating such products. Most land data assimilation approaches are based on an assumption of temporally-white and Gaussian-distributed errors forms (Burgers et al., 1998). Therefore, a thorough examination of soil moisture retrieval error structure is crucial for not only properly describing their error

61 characteristics but also their potential implementation within a land data assimilation system

62 (Crow and Van den Berg, 2010).

63   Gridded satellite-based soil moisture retrievals are based on the sampling of adjacent

64 footprints within the same orbital overpass. Three commonly used interpolation algorithms are:

65 drop-in-bucket, nearest neighbor, and inverse-distance-squared methods (Chan et al., 2012). The

66 choice of interpolation algorithm affects the effective antenna pattern of the spatial support

67 associated with a particular grid box. For the Soil Moisture Active Passive (SMAP) mission, the

68 averaged half-power beam-width field-of-view (FOV) size of the inverse-distance-squared

69 approach is about 40 km. In addition, radiation outside the half-power beam-width can contribute

70 to the signal – suggesting that the gridded signal may include significant radiance contributions

71 from emitters outside the grid (Jackson et al., 2010). For polar-orbiting satellites with an exact

72 repeat cycle there are periodic variations in the spatial support of individual grids (due to day-to-

73 day variations in the exact footprint-averages underlying each grid cell). Over highly

74 heterogeneous regions, the impact of this periodic sampling may become more pronounced and

75 periodic errors may arise which are related to the periodicity of the sampling pattern.

76   Additionally, passive microwave observations are potentially contaminated by man-made

77 radio frequency interference (RFI). RFI can obscure (relatively weaker) geophysical emission

78 associated with land source variables like soil moisture (Daganzo-Eusebio et al., 2013; Njoku et

79 al., 2005). In addition to the spatial heterogeneity in natural land surface signals, RFI sources

80 observed over land areas are typically fixed in space (Njoku et al., 2005) which may lead to

81 periodic errors in satellite-based retrievals as these sources are re-sampled periodically. From this

82 point of view, a satellite-derived soil moisture product with consideration of the contributing factor

83 of RFI should be analyzed to expose the origins of periodic errors.

84   In practice, a simple *ad hoc* low pass filter (i.e., a 5-day moving average) adopted by

85   Wagner et al. (2007b) and Draper et al. (2009) has been shown to slightly improve the quality of

86   satellite-based soil moisture retrievals. Nonetheless, this empirical method is arbitrary and only

87   effective for dampening very short-term fluctuations (i.e., 2-day periodic errors). Recent

88   experimental studies have shown that analyzing the soil moisture time series in the frequency

89   domain can provide supplementary insights with regard to its conjugate time domain (Katul et al.,

90   2007). For example, Du (2012) used the high-pass Fourier filter to keep small temporal scale soil

91   moisture signals in the directly observed emissivity time series, while filtering out the mixture

92   signals of vegetation phenology in the low frequency component (Moody and Johnson, 2001;

93   Scharlemann et al., 2008) and long-term soil moisture trends. However, such a method requires

94   not only the accurate extraction of high-frequency soil moisture signals from sensor direct

95   observations, but also the availability of an accurate long-term climatology from land surface

96   models or existing satellite-based soil moisture product. On the other hand, Su et al. (2013a)

97   applied a band-stop filter to remove the identifiable stochastic and systematic errors in high-

98   frequency regime and then a low-pass Wiener filter for preserving the long-term temporal mean

99   and variance. This approach is more physically realistic and based on the rationale that small time

100   scale soil moisture dynamics can be simplified into incoming precipitation and water loss process

101   with brown-like spectrum (Katul et al., 2007; Su et al., 2013a).

102   However, the application of any filter comes at the risk of information loss. For example,

103   when blindly applying the band-stop filter, high-frequency signal components related to rapid soil

104   moisture changes following intense rainfall events can also be attenuated. Therefore, the accurate

105   *a priori* identification of land surface conditions associated with spurious high frequency

106   resonances is beneficial for efficient and flexible application of the band-stop filter.

107   To examine the plausible reasons behind the existence of high-frequency peaks and

108   improve our understanding of errors in the satellite-derived soil moisture time series, this study

109   will focus primarily on the most prominent and consistent periodicity (8-day) existing in an

110   AMSR-E soil moisture retrieval product. The spatial distribution of such a periodic error will be

111   inter-compared to measures of land surface spatial heterogeneity. Section 2 presents the satellite-

112   derived soil moisture product from the passive microwave AMSR-E sensor via the Land Parameter

113   Retrieval Model (LPRM) retrieval algorithm, the spectral analysis of soil moisture, and our peak

114   detection method. Three straightforward heterogeneity indicators, based on: microwave brightness

115   temperature, land cover types, and long-term averaged Normalized Difference Vegetation Index

116   (NDVI), are then proposed for characterizing spatial variability along the land surface. Section 3

117   evaluates the spectral characteristics of soil moisture retrievals and explains their relationship with

118   these heterogeneity indicators. Further discussion of concerns and potential implications is

119   provided in section 4, and final conclusions are presented in section 5.

120

II. Materials and methods

122   A long-term soil moisture product is necessary in order to robustly investigate periodic

123   errors in satellite-derived soil moisture time series. Among various microwave sensors and

124   missions, the AMSR-E sensor onboard the National Aeronautics and Space Administration

125   (NASA) Aqua provides the longest currently-available source of soil moisture data (i.e., from June

126   2002 to October 2011) from a single sensor and is therefore the primary focus of this study.

127

2.1. AMSR-E soil moisture product and LPRM retrieval model

2.1.1 AMSR-E basic information

130   The AMSR-E sensor was a six-frequency dual-polarized passive microwave radiometer,

131   onboard the NASA Aqua satellite with a 16-day exact repeat cycle. With a sun-synchronous orbit

132   at an altitude of 705 km, AMSR-E scans the Earth's surface at 1:30 a.m. (descending)/1:30 p.m.

133   (ascending) local equator overpass time and an incidence angle of 55°. AMSR-E provided a nearly

134   nine-and-a-half-years long-term measurement time series from June 2002 to October 2011.

135   Among its six microwave frequency bands, the spatial resolutions of footprint measurements at

136   6.9 GHz (C-band), 10.7 GHz (X-band), and 36.5 GHz (Ka-band) were 74 ×43 km, 51×30 km,

137   and 14×8 km, respectively (Njoku et al., 2003).

138   Several soil moisture retrieval algorithms have been developed for AMSR-E brightness

139   temperature (T_B) data. Here, surface soil moisture (~2 cm) and vegetation optical depth are

140   retrieved simultaneously from C-band T_B via the LPRM (see below for further details). In areas

141   with significant RFI such as the contiguous United States (CONUS), Japan, and India, LPRM

142   switches to X-band. Figure 1.a and 1.b show the distribution maps of bands that have been utilized

143   for soil moisture retrieval. Regardless of the band used, AMSR-E ascending and descending half-

144   orbits are separately re-sampled from their original footprint resolution to a regular quarter degree

145   grid and then processed through LPRM to retrieve soil moisture (see below).

146   *2.1.2 Land Parameter Retrieval Model*

147   LPRM uses a forward modeling optimization procedure to solve a radiative transfer

148   equation without the need for parameter calibration and other biophysical measurements. The

149   physically-based LPRM (De Jeu and Owe, 2003; Meesters et al., 2005; Owe et al., 2001) has been

150   successfully applied to retrieve surface soil moisture from space-borne passive microwave

151   observations including AMSR-E (Owe et al., 2008) and SMOS (De Jeu et al., 2009; Van der

152   Schalie et al., 2015; Van der Schalie et al., 2016). Moreover, the AMSR-E LPRM product has

153 been well-validated with *in situ* campaigns (Brocca et al., 2011; De Jeu et al., 2008; Draper et al.,

154 2009; Su et al., 2013b) and thoroughly assessed in previous studies (Al-Yaari et al., 2014; Dorigo

155 et al., 2010; Draper et al., 2012; Rebel et al., 2012). Here, version 5 of the AMSR-E LPRM soil

156 moisture product is collected from January 2003 to October 2011.

157   The LPRM algorithm can simultaneously retrieve surface soil moisture and vegetation

158 optical depth (VOD) from passive microwave observations using both horizontally- and vertically-

159 polarized T_B data. The retrieval scheme is based on solving a radiative transfer model (Mo et al.,

160 1982) via a nonlinear iterative optimization procedure. The radiation emission T_b measured over

161 a land surface with vegetation canopy can be described as

162 $$T_{b(P)} = T_S e_{r(P)}\Gamma_V + (1 - \omega)T_C(1 - \Gamma_V) + (1 - e_{r(P)})(1 - \omega)T_C(1 - \Gamma_V)\Gamma_V \qquad (1)$$

163 where the subscript P is H for horizontal or V for vertical polarization, T_S the thermodynamic soil

164 temperature, $e_{r(P)}$ the rough surface emissivity, Γ_V the vegetation transmissivity, ω the single

165 scattering albedo, and T_C the canopy temperature. The above equation represents three terms: the

166 radiation emanated from the underlying soil as attenuated by the canopy, the upward radiation

167 directly from the overlying vegetation, and the downward radiation from the vegetation (reflected

168 by the soil and further attenuated by the vegetation).

169   The rough surface emissivity is calculated for both polarizations using the emissivity model

170 developed by Wang and Choudhury (1981)

171 $$e_{r(H)} = 1 - ((1 - Q)R_{s(H)} + QR_{s(V)})e^{-hcos(u)} \qquad (2)$$

172 where Q and h are the polarization mixing factor and empirical roughness, respectively, and both

173 are dimensionless parameters. The smooth surface reflectivity R_s is a function of dielectric

174 constant k and satellite observational incidence angle u and is calculated using the Fresnel

175 equations. Furthermore, the dielectric constant k is estimated via the Wang-Schmugge dielectric

176   mixing model (Wang and Schmugge, 1980). Equation 2 is written for H polarization emissivity.

177   For V polarization results, the polarization signs should be switched.

178   The vegetation transmissivity Γ_V is defined in terms of the VOD τ_V and incidence angle u

179   as

180    $$\Gamma_V = \exp\left(\frac{-\tau_V}{\cos(u)}\right) \tag{3}$$

181   The VOD τ_V is directly related to the canopy density, or more specifically, the vegetation water

182   content. Derived by Meesters et al. (2005), the VOD is a function of k and the Microwave

183   Polarization Difference Index (*MPDI*)

184    $$MPDI = \frac{T_{b(V)} - T_{b(H)}}{T_{b(V)} + T_{b(H)}} \tag{4}$$

185   where *MPDI* is calculated directly from observed brightness temperatures. By normalizing for

186   temperature dependence, the *MPDI* becomes more highly-related to the dielectric properties of the

187   radiating body including both the canopy and soil emissions (Owe et al., 2008).

188   Regarding the thermodynamic conditions of vegetation and soil, a further assumption in

189   the LPRM algorithm is that the soil temperature and canopy temperature are in isothermal

190   equilibrium

191    $$T_S = T_c = T \cong aT_{b(V)}^{Ka} + b. \tag{5}$$

192   For AMSR-E, T is derived from the accompanying Ka-band T_b at V polarization (Holmes et al.,

193   2009). Atmospheric contributions to satellite observed T_B are also taken into account following

194   Owe et al. (2008).

195

196   ***2.2. Ancillary dataset***

197   *2.2.1 International Soil Moisture Network*

198   The International Soil Moisture network (ISMN) has assembled over 50 operational and

199   experimental soil moisture networks worldwide, providing a global *in situ* soil moisture database

200   with uniform data format and pre-processing quality flags (Dorigo et al., 2013). While most of the

201   networks are located in northern America and Europe, some regions in Asia and Australia are also

202   covered. Detailed information about the ISMN is reported in Dorigo et al. (2011) and Gruber et al.

203   (2013). The ISMN dataset was downloaded from http://ismn.geo.tuwien.ac.at in February 2017.

204   For direct comparison with AMSR-E LPRM soil moisture product, these sparsely

205   distributed *in situ* soil moisture records are analyzed in the frequency domain as well. The ISMN

206   soil moisture is originally recorded along with Coordinated Universal Time (UTC) time and has

207   been converted to local solar time before next processing. To be consistent with the overpass time

208   of AMSR-E, records are extracted at 02:00 p.m. and 01:00 a.m. for ascending and descending half-

209   orbits, respectively. Observations are masked using the quality flag (identified as 'good' with 'G')

210   and stations located within the same quarter degree box are averaged for simplicity. For example,

211   there are three networks of which 55 stations are collocated within a quarter degree grid (latitude:

212   38.375° N, longitude: 120.875° W), namely COSMOS, FLUXNET-AMERIFLUX, and

213   SOILSCAPE. However, only three stations provided measurements during our study period and

214   are averaged accordingly. Note that the point-scale soil moisture observation cannot fully represent

215   the footprint satellite retrieval and the sampling depth may also introduce differences. Strategies

216   have been proposed for minimizing the systematic differences between ground-based

217   measurement and satellite-based retrievals, such as computing anomalies through subtracting a

218   moving window averaging-based climatology (Dorigo et al., 2015; Gruber et al., 2013). However,

219   since the *in situ* soil moisture is used only to help identifying spectral spectral peaks in AMSR-E

220   LPRM soil moisture retrievals, these strategies have not been applied here.

221 *2.2.2 Land cover—GlobeLand30*

222   Several global land cover maps derived from multiple satellite sensors are currently

223 available. The sensitivity of microwave emissivity to soil moisture varies with different land cover

224 variables – in particular, vegetation optical depth. High spatial resolution surface land cover maps

225 can thus provide sub-pixel heterogeneity information for coarse resolution soil moisture products.

226 However, the isolation of highly mixed land cover types is cumbersome and beyond the scope of

227 this study. Therefore, the 30-meters high resolution GlobeLand30 dataset, based on Landsat data

228 (Chen et al., 2015), is merely included for visual interpretation of the spatial heterogeneity within

229 the quarter degree grid of AMSR-E LPRM soil moisture retrievals. According to previous

230 independent accuracy assessments, the GlobeLand30 has demonstrated an overall accuracy of over

231 80% (Brovelli et al., 2015). It was downloaded from http://globallandcover.com in January 2017.

232 *2.2.3 Normalized Difference Vegetation Index (NDVI)—MODIS*

233   The Moderate Resolution Imaging Spectroradiometer (MODIS) monthly NDVI

234 (MOD13C2) product is obtained from January 2003 to December 2011. To be consistent with

235 AMSR-E LPRM soil moisture retrievals, it has been spatially-aggregated from its original 0.05°

236 grid to a regular 0.25° resolution. A long-term averaged global NDVI distribution map is then

237 generated by averaging all quarter-degree monthly data. The MOD13C2 dataset was downloaded

238 from   https://lpdaac.usgs.gov/dataset_discovery/modis/modis_products_table/mod13c2_v006

239 during May 2017.

240 *2.2.4 Land cover type—MODIS*

241   In addition to the high resolution land cover from the GlobeLand30 product, a dominant

242 land cover type map at lower spatial resolution (0.05°) is acquired from the MODIS yearly Land

243 Cover Type Climate Modeling Grid (MCD12C1) product in 2011. This product also provides the

244 sub-grid frequency distribution of land cover types. Three classification schemes are included and

245 the primary International Geosphere Biosphere Programme (IGBP) land cover scheme is selected

246 for further analysis. IGBP contains 17 land cover classes and has been re-classified into 9 classes

247 before spatially-aggregated to regular quarter degree (0.25°). They are: Water, Forest, Shrublands,

248 Grasslands, Cultivated Land, Wetlands, Artificial Surfaces, Permanent Snow and Ice, and

249 Bareland. Percentages of difference land cover types are summed for each quarter-degree box and

250 normalized to [0,100]. The MCD12C1 dataset was downloaded from https://lpdaac.

251 usgs.gov/dataset_discovery/modis/modis_products_table/mcd12c1 during May 2017.

252

2.3. Spectral frequency analysis and peak detection method

253

254 *2.3.1 Power spectral density estimation*

255 The dynamics of soil moisture is an outcome of interactions between incoming

256 precipitation, canopy interception, evapotranspiration, surface runoff, lateral flow and

257 groundwater. The near-surface soil moisture time series consists of both a long-term climatology

258 (low frequency) and short-term anomaly (high frequency) components (Entin et al., 2000). The

259 long-term climatology originates from seasonally varying precipitation and solar radiation and can

260 be affected by the vegetation phenology, climate change, and instrument drift for satellite

261 observations. In contrast, the short-term anomalies represent the process of rainfall instances and

262 dry-down events and are valuable for analyzing short-term weather extremes (Katul et al., 2007;

263 Wu and Dickinson, 2004). However, this short-term information is usually contaminated by

264 observational noises and systematic errors. Here, we focus on the periodic error in the high-

265 frequency regime which may be introduced by the satellite orbiting pattern and/or gridding

266 approach.

267   Following the approach of Su et al. (2013a; 2015), the power spectral density (PSD, in unit

268   of m^6/m^6 24hr/rad) of AMSR-E LPRM soil moisture retrievals at a given grid is estimated using

269   the Welch's averaged modified periodogram method. This method computes a modified

270   periodogram for each temporal segment separated by a moving Hamming window and averages

271   over all estimates to produce a single PSD. Note that the size of Hamming window can play a role

272   in determining the PSD estimation. Wider Hamming windows tend to produce higher spectral

273   resolution in the estimated PSD but greater uncertainty in the amplitude estimation, while shorter

274   windows provide coarser spectral resolution but with lower uncertainty in amplitude. The impact

275   of Hamming window size on key results will be clarified when describing the peak detection

276   method in section 2.3.4.

277   Another issue with PSD estimation is satellite overpass time. AMSR-E has a ascending

278   half-orbit at 1:30 p.m. and descending half-orbit at 1:30 a.m. Considering that the FOV and near-

279   surface thermal conditions (more specifically, the temperature contrast across the soil-vegetation-

280   air interface) are quite different for these two half-orbits, soil moisture retrievals from ascending

281   and descending overpasses have been separately analyzed with periodic temporal sampling along

282   a 24 h interval.

283   In applying the Fourier transform to stationary time series, most standard PSD estimation

284   algorithms – including Welch's method – require an evenly sampled dataset in time. However,

285   temporal data gaps in passive microwave satellite-derived soil moisture product are inevitable –

286   primarily due to the satellite orbits, dense vegetation, RFI contamination, and masking for frozen

287   soil conditions. In this particular case, AMSR-E LPRM soil moisture retrievals are masked if the

288   complementary VOD levels exceeded 0.8—a level at which the soil radiation is substantially

289   masked out by the canopy (Owe et al., 2008; De Jeu et al., 2008; Parinussa et al., 2011). Further

290 masking has been conducted for grids with significant RFI contamination (Li et al., 2004) and for

291 frozen soil conditions. In order to produce evenly-spaced data after the application of this masking,

292 the 1-D Discrete Cosine Transform (DCT) method (Garcia, 2010) is applied for infilling missing

293 values in the AMSR-E LPRM soil moisture time series. In this study, only grids with less than 365

294 observations during the 9-years experiment period (11%) are omitted to preserve sufficient spatial

295 coverage for global analysis with indication of highly in-filled regions. Figure 1.c and Figure 1.d

296 show the fraction of in-filled data in the AMSR-E LPRM soil moisture product for both descending

297 and ascending retrievals. Due to the generally warmer surface conditions during the ascending

298 (01:30 p.m.) half-orbit (Holmes et al., 2015), the fraction of data gaps in descending overpasses is

299 slightly higher than its ascending counterpart. Additional discussion and an assessment of the

300 infilling method can be found in section 4.2 and section A of the supporting materials.

301
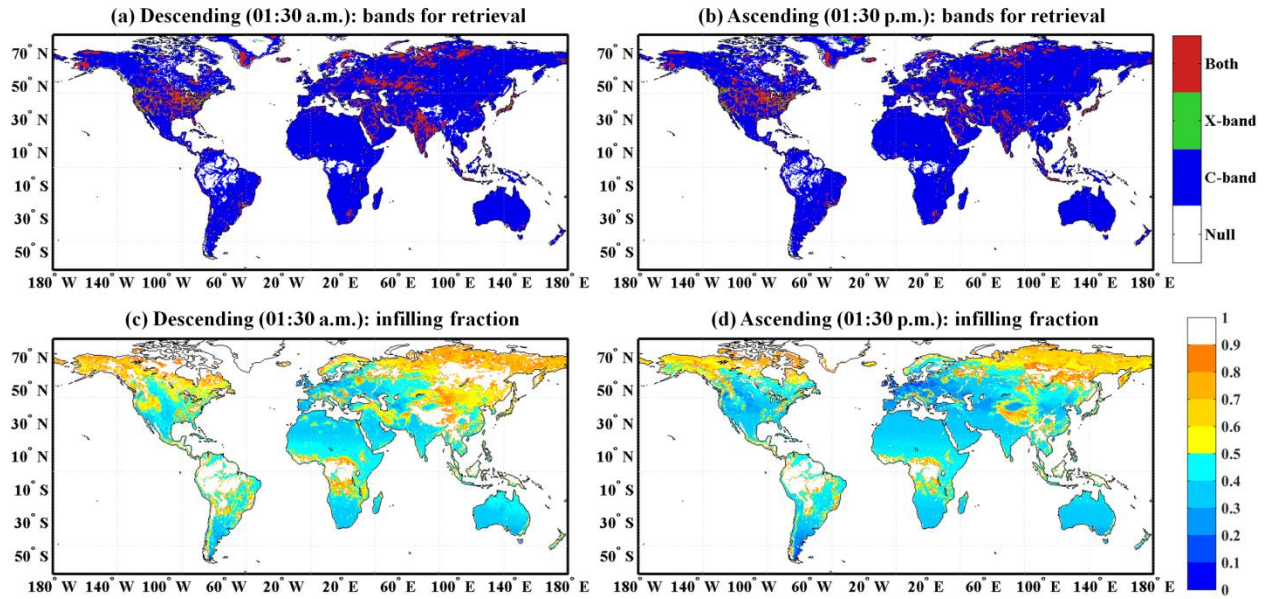
302 **Figure 1.** Spatial distribution maps of applied bands for AMSR-E LPRM soil moisture retrieval (upper row) and

303 fraction of in-filled data for the period 2003 – 2011 (bottom row): (a) and (c) for descending; (b) and (d) for ascending

304 overpasses, respectively.

305 *2.3.2 Spectrum characteristics of soil moisture time series*

306   Figure 2 shows the AMSR-E LPRM and ISMN *in situ* soil moisture time series from

307   January 2003 to October 2011 for a single 0.25° grid (latitude: 38.375° N, longitude: 120.875° W).

308   Corresponding PSDs are estimated with two Hamming window sizes (i.e., 1.0 and 8.8 in units of

309   year).

310   According to Katul et al. (2007), the soil water balance model dictates that the soil moisture

311   time series exhibits a Brownian spectrum with more energy at lower frequency and a decrease in

312   power with increasing frequency (Figure 2.c). Comparing the PSDs of footprint AMSR-E LPRM

313   soil moisture retrievals and point-scale *in situ* observations, significant discrepancies exist at high

314   frequencies. In particular, the relatively flat power distributions of AMSR-E LPRM soil moisture

315   for $T<10^3$ h reflect high-frequency noise, which can be introduced by various short-term stochastic

316   processes contributing to retrieval errors (Su et al., 2013a). Note that – based on a thorough

317   exploration over various grids with *in situ* soil moisture observations – the grid demonstrated here

318   is representative for a spectral comparison between ground-based measurements and satellite-

319   derived soil moisture retrievals.

320   Importantly, several distinct resonant peaks with periods ranging between 2 to 16 days are

321   sitting on the AMSR-E flat noise floor (Figure 2.d). Given the lack of known physical processes

322   capable of producing such harmonics, these peaks are likely spurious signals characterized by

323   periodic increases in power with these time intervals. Without consideration of the long-term

324   satellite orbit drift, the repeat cycle of AMSR-E is 16 days which means that the sensor observes

325   exactly the same region every 16 days. Within this 16-day period, there are periodic variations in

326   the locations of antenna footprints sampled to capture a grid-cell mean (as shown in Figure 3). Our

327   hypothesis is that this kind of periodic sampling pattern can generate spectral peaks within highly

328 heterogeneous regions. If true, it implies that spectral peaks can be connected to strong – and

329 temporally stable – patterns of land surface heterogeneity.
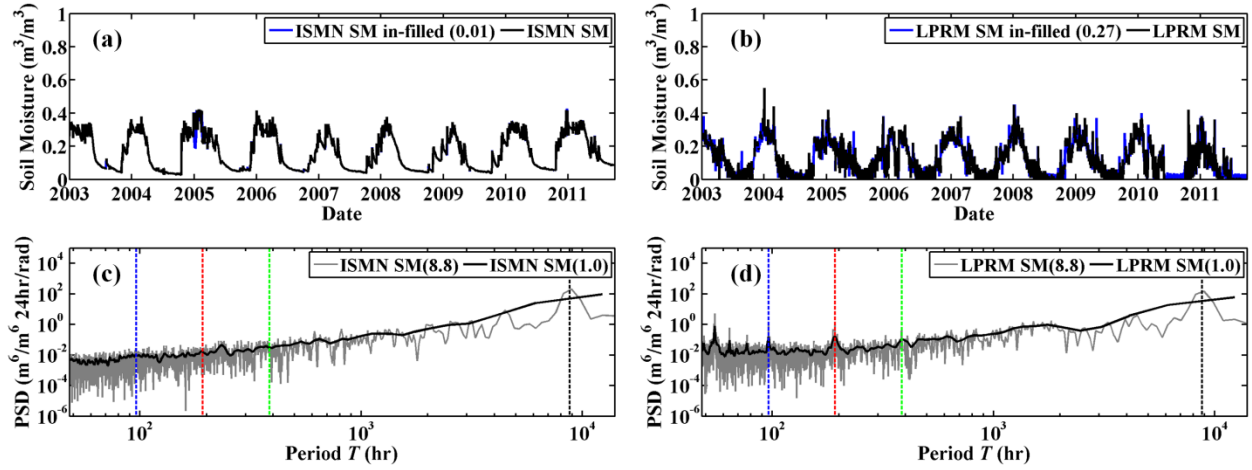
331 **Figure 2.** The soil moisture time series (a and b) and corresponding power spectral density (PSD, c and d) of both

332 ISMN *in situ* and AMSR-E LPRM soil moisture data at the ascending overpass time (01:30 p.m.). The infilling

333 fractions of soil moisture data are shown in the brackets and the Hamming window sizes for PSD estimation inside

334 the brackets are in units of year. From left to right, the dotted vertical lines represent periods at 4-day (blue), 8-day

335 (red), 16-day (green), and 365-day (black).
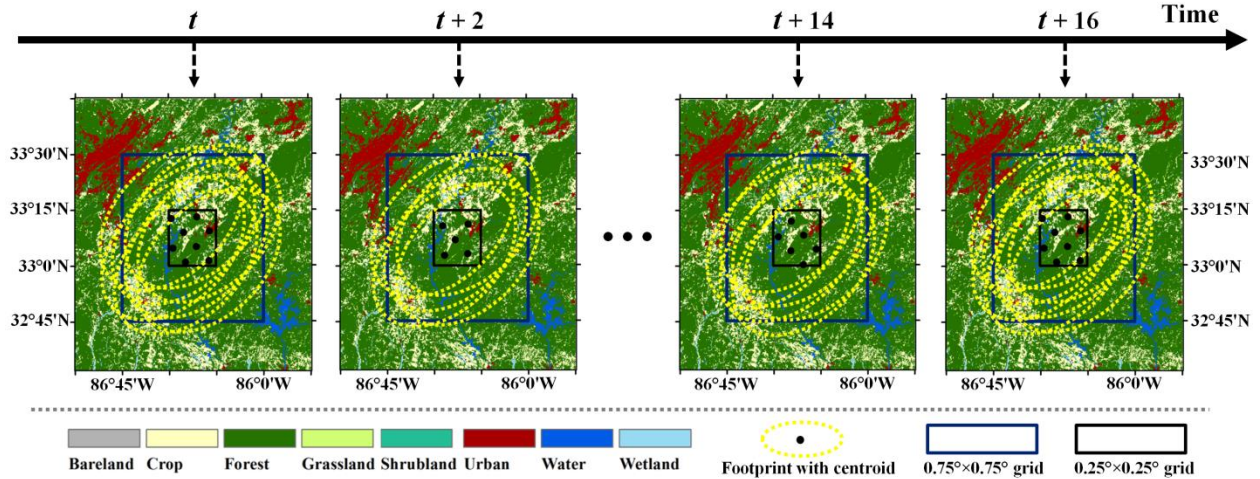
337 **Figure 3.** An illustration of the time-varying effective spatial support for a single quarter degree grid (centered at

338 33.125° N, 86.375° W and outlined with a black square) where multiple adjacent footprints (yellow dotted ellipses)

339 within the same orbital overpass are averaged. The background land cover maps are projected in World Geodetic

16

340   System (WGS) 1984 Universal Transverse Mercator (UTM) zone 16 North system. Comparing time t and $t + 16$, the

341   satellite observes exactly the same region.

342   *2.3.3 Examining the occurrence of periodic errors*

343   To further facilitate the physical interpretation of the occurrence of high-frequency peaks,

344   a simplistic synthetic experiment monitoring the periodic sampling pattern of satellite swaths over

345   different land cover characteristics has been conducted following the approach illustrated in Figure

346   4. In particular, an Antecedent Precipitation Index (API) model is applied to generate synthetic

347   soil moisture $SM_{t,i}$ (mm, in a dimension of water depth) for each sub-grid i at time t

348    $$SM_{t,i} = \gamma SM_{t-1,i} + P_t \qquad i = 1, \dots, n \tag{6}$$

349   where γ is a dimensionless API loss coefficient and assumed to be a constant value as 0.95; n is

350   the total number of sub-grids which is set to 9 (3-by-3), and P_t (mm) represents the daily

351   accumulation depth of random rainfall expressed in dimensions of water depth and generated from

352   the exponential distribution with mean of 25 mm.

353   In total, there are five synthetic scenarios (see Figure 4). The synthetic "True" soil moisture

354   is generated directly through the API model without any assumed observational error, while mean-

355   zero Gaussian distributed random observational error with a standard deviation of 10 mm is added

356   to the other four cases. With the consideration of spatial heterogeneity, a long-term bias in soil

357   moisture within the 3-by-3 grid box is set up as a random pattern from a mean-zero normal

358   distribution with a standard deviation of 20 mm. This long-term bias is meant to represent the

359   systematic land cover and/or soil physical property variations. Furthermore, the periodic sampling

360   pattern of satellite footprints is constructed by repeating equally-weighted averaging with different

361   combinations of sub-grids (to account for the drop-in-bucket method use in the AMSR-E LPRM

362   product). In accordance with AMSR-E, the repeat cycle is set to 16-days. Through the combination

363   of these two conditions, four experiments are generated (see Figure 4). Here, the differences in

364   mean and standard deviation settings among precipitation, soil moisture observational error and

365   long-term bias only represent their scaling differences and proportionally rescaling these statistical

366   moments does not affect presented results. Before the spectral frequency analysis, five synthetic

367   soil moisture time series (four Cases and "True") are normalized respectively from their original

368   climatology to be mean-zero with a standard deviation of one. These synthetically-generated

369   results will be used to enhance our understanding of peak-generating processes within our real-

370   data analysis. Results from these synthetic experiments will be presented in section 3.1.

371
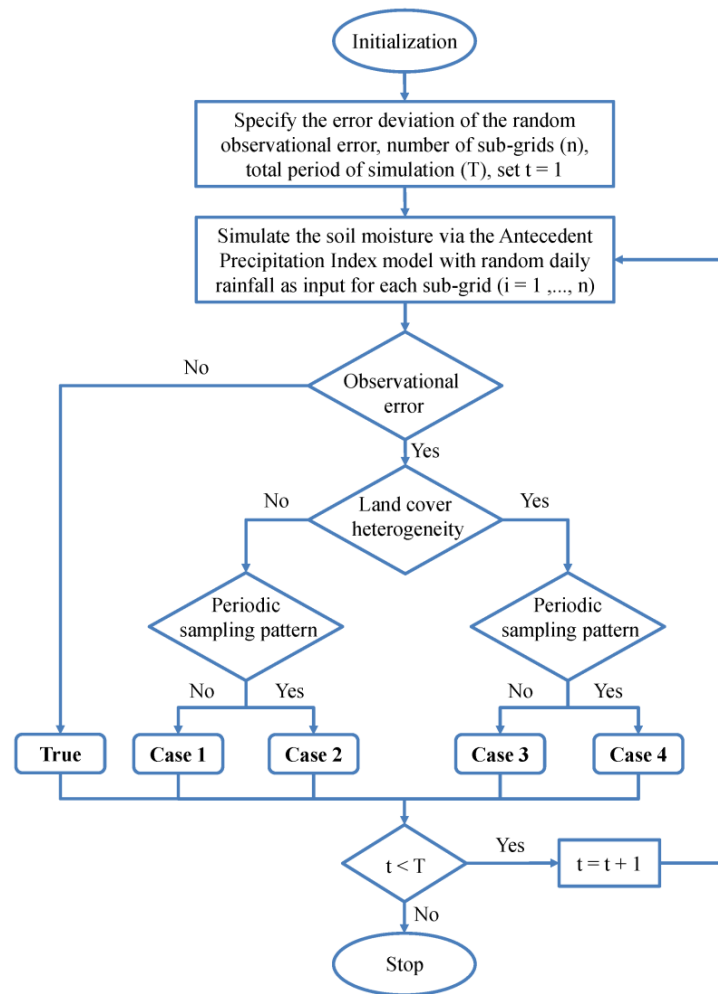
372   **Figure 4.** Flowchart of synthetic experiments which examine the combined impact of land surface heterogeneity and

373   periodic orbital sampling pattern on producing spectral harmonics.

18

374   *2.3.4 Detection of 8-day periodic error*

375   With a Brownian spectrum of soil moisture, the increase in power with decreasing

376   frequency may hinder detection of 16-day peaks in cases where the true soil moisture signal is

377   stronger than the 16-day resonance. In addition, spectral peak features in higher frequencies can

378   be difficult to be distinguished from the high-frequency noise. Therefore, despite the fact that

379   AMSR-E LPRM soil moisture retrievals demonstrate several spectral resonances, we will focus

380   on 8-day peaks as they represent the most prominent and consistent periodic signal. Detailed peak

381   detection procedures are described below.

382   To start, the PSD estimations of AMSR-E LPRM soil moisture product are conducted using

383   the Welch's method with different Hamming window sizes. As stated earlier, the window size

384   determines the amplitude accuracy and frequency resolution of the PSD. To reach a compromise

385   between them and provide sufficient support for detecting periodicity in high frequency, the

386   window size is varied between 270 to 360 days at 10-day intervals. Thus, for each grid, there are

387   ten separate estimates of PSD. These PSDs and corresponding frequency series are then

388   transformed into logarithm space for further analysis. Polynomial interpolation is used to remove

389   the background Brownian shape of PSD, allowing for more accurate detection of the peaks. For

390   detecting the most prominent and consistent 8-day peaks, two thresholds are employed: a) the

391   minimum peak height is no less than 3-sigma (standard deviation) of the de-trended PSD

392   estimations; and b) the 8-day peaks are repeatedly detected by at least 5 times (out of the 10

393   Hamming window sizes considered at each grid). In addition, the same peak detection approach is

394   applied for AMSR-E brightness temperature T_B-derived parameters as described in the following

395   section 2.4.1.

396

397 *2.4. Land Surface Heterogeneity indicator*

398   The land surface characteristics are extremely variable in both space and time. Our strategy

399   is based on applying the best available global descriptions of land surface characteristics from both

400   microwave and visible/near-infrared remote sensing and comparing these patterns to maps of 8-

401   day spectral peak presence. Naturally, all heterogeneity descriptions have resolution limitations

402   which prevent them from capturing all sub-pixel scale heterogeneity (Lakhankar et al., 2009b).

403   *2.4.1 T_B-derived heterogeneity indicator*

404   The AMSR-E T_B data are re-sampled onto regular quarter degree grid using a drop-in-

405   bucket approach. Quarter degree grid-scale averages are acquired by averaging all footprints –

406   across various scans and swath cycles – whose geographic centers fall within a grid box for a given

407   day. Thereby, the spatial coverage of the effective radiating body can extend beyond the

408   boundaries of each grid box. In fact, according to Jackson et al. (2010), the main contribution of

409   radiation can come from a $0.75° × 0.75°$ box centered at each quarter degree grid. Therefore,

410   mirroring the land surface parameterization of the LPRM algorithm, a T_B-derived heterogeneity

411   indicator (TB-HI) is proposed to characterize the spatial heterogeneity of the underlying land

412   surface (within a centered $0.75° × 0.75°$ box) for several adjoining satellite footprints within the

413   same orbital overpass

$$H_{3×3}^{TB} = H_{3×3}^{MPDI} + H_{3×3}^{MWE} + H_{3×3}^{TEMP} \tag{7}$$

415   where

$$H_{3×3}^{MPDI} = std[\log(MPDI)_{i,j}] \equiv std\left[\log\left(\frac{1}{N}\sum_{t=1}^{N}\frac{T_{B(V),t}^{C}-T_{B(H),t}^{C}}{T_{B(V),t}^{C}+T_{B(H),t}^{C}}\right)_{i,j}\right] \quad i,j\sim(1,2,3) \tag{8}$$

$$H_{3×3}^{MWE} = std[\log(MWE)_{i,j}] \equiv std\left[\log\left(\frac{1}{N}\sum_{t=1}^{N}\frac{T_{B(H),t}^{C}}{T_{B(V),t}^{Ka}}\right)_{i,j}\right] \quad i,j\sim(1,2,3) \tag{9}$$

418 $$H_{3\times3}^{TEMP} = std\left[\log\left(\frac{1}{N}\sum_{t=1}^{N}T_{B(V),t}^{Ka}\right)_{i,j}\right] \quad i,j{\sim}(1,2,3) \tag{10}$$

419 and $std[{\sim}]$ represents the mathematic operation of calculating standard deviation for a 3×3 box

420 (i.e., $0.75°{\times}0.75°$). In Equations (8–10), i and j are the grid index within the 3×3 box, and N is

421 the total number of sampled time steps. $H_{3\times3}^{MPDI}$ is calculated based on the AMSR-E C-band T_B data

422 and can be a reflection of both the soil and canopy information (Owe et al., 2001). Moreover, the

423 effective emissivity ($MWE = T_{B(P)}/T$) is used in Equation 9 to capture the heterogeneity in

424 emissivity while the Ka-band T_B at V represents the effective surface temperature T. The spatial

425 variation of temperature is also taken into account using Equation 10. For simplicity, fixed values

426 of $MPDI$, MWE, and $T_{B(V)}^{Ka}$ are assigned to water bodies: $MPDI = 0.2$ (Chen et al., 2011),

427 $MWE = 0.5$ (Grody, 1993; Weng, 2010), $T_{B(V)}^{Ka} = 220$ (Lin et al., 1998). The ranges of these

428 heterogeneity components are slightly different, thus global normalization has been conducted for

429 each component and $H_{3\times3}^{TB}$ (unit-less) is further normalized into $[0,100]$ after arithmetic

430 summation. Note that this heterogeneity indicator is computed directly from the AMSR-E

431 observed T_B data without any other auxiliary biophysical information sources and can be adapted

432 to other microwave satellite or retrieval algorithms as well. For example, C-band $T_{B(P)}^{C}$ could be

433 replaced with L-band $T_{B(P)}^{L}$ acquired from the SMOS and SMAP missions, while surface

434 temperature data could also potentially be derived from land surface model output.

435 *2.4.2 NDVI-derived heterogeneity indicator*

436   Vegetation canopy plays an important role in observing and retrieving soil moisture from

437 space-borne platforms (Jackson et al., 1982). NDVI is a simple index of vegetation density which

438 can be applied for depicting the land surface characteristics. To take into account the canopy, a

439   straightforward NDVI-derived heterogeneity indicator (VI-HI) is proposed with a form similar to

440   TB-HI

441
$$H_{3\times3}^{VI} = std\left[\left(\tfrac{1}{N}\sum_{t=1}^{N} NDVI_t\right)_{i,j}\right] \ i,j\sim(1,2,3) \tag{11}$$

442   where the standard deviation ($std[\sim]$) of NDVI is calculated for a 3×3 box centered at each

443   quarter degree grid. This indicator characterizes the spatial variability of vegetation density over

444   the average main-beam FOV of AMSR-E.

445   *2.4.3 Land cover-derived heterogeneity indicator*

446   Different land cover types can demonstrate distinct physical characteristics with varying

447   temporal climatology. Regions with various land cover types can be quite heterogeneous with

448   regard to satellite-based soil moisture retrieval. Therefore, a land cover-derived heterogeneity

449   indicator (LC-HI) is defined as the number of individual land cover types contained within a single

450   0.75°×0.75° box for each quarter degree grid

451
$$H_{3\times3}^{LC} = \left|\left(\langle LC_k^{Perc} \geq 10\rangle \cup \langle 10 > LC_{Water}^{Perc} > 0\rangle\right)_{i,j}\right| \ k\sim(1,9) \ \ i,j\sim(1,2,3) \tag{12}$$

452   where $|\sim|$ denotes the cardinality operator, LC_k^{Perc} represents the grid area in percent classified as

453   land cover type k (out of nine classes), and LC_{Water}^{Perc} is the percentage classified as Water. Open

454   water, with its high dielectric constant, has a profound impact on the microwave emission and even

455   small fractions of open water may greatly alter the T_B observations (Loew, 2008). In this case, LC-

456   HI will increase 1 if there is open water within the 3×3 box. The other land cover classes are only

457   taken into account when their percentages are larger than 10%.

458

III. Results

460   Our main interest is examining the most prominent and consistent spectral peaks generated

461   from AMSR-E's periodic sampling pattern and the relationship between theses peaks and the

462 spatial heterogeneity of the corresponding land surface. To physically explore the occurrence of

463 high frequency spectral peaks, both the synthetic experiment and a detailed site-specified analysis

464 are discussed first. Subsequently, the global distribution of the 8-day periodic errors, and their

465 relationship with the spatial heterogeneity indicators introduced in section 2.4, is presented.

466 *3.1 Synthetic experiments*

467 Figure 5 demonstrates the PSD estimations of five synthetic soil moisture time series (as

468 described in section 2.3.3). Compared to the "True" scenario, both Case 1 and Case 3 show quite

469 similar spectral characteristics suggesting that the land cover heterogeneity alone cannot lead to

470 high-frequency peaks without periodic sampling pattern. While both Case 2 and Case 4 exhibit a

471 moderate noise floor over the "True" soil moisture for periods between 2- and 4-days. Particularly,

472 significant frequency peaks are exposed when the periodic sampling pattern is combined with

473 spatial heterogeneity in Case 4. The results suggest that, in the absence of either the spatial

474 heterogeneity or periodic sampling patterns, high frequency peaks cannot be produced.

475
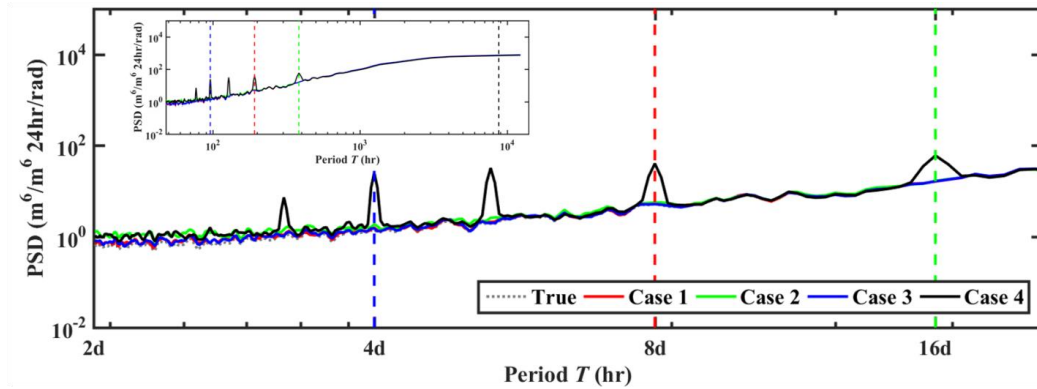
476 **Figure 5.** High-frequency PSD for soil moisture time series generated by the synthetic "True" case and the synthetic

477 "satellite-based" Cases 1–4. The Hamming window size is set equal to 365 days. The entire PSDs (including lower-

478 frequency components) are shown in the upper left corner. From left to right, the colored dashed vertical lines represent

479 4-day, 8-day, 16-day, and 365-day periods. Note that the PSDs of the 'True' case and Cases 1–3 are virtually

480 indistinguishable.

481   Additionally, the influence of different re-gridding methods on the occurrence of spectral

482   peaks has been explored. All PSD estimations of three re-gridded soil moisture time series have

483   shown notable spectral peaks, indicating that the peaks are result for a combination of periodic

484   sampling patterns and stable spatial heterogeneity – regardless of exact re-gridding method applied

485   (see section B of the supporting materials for further discussion).

486   *3.2. Site-specified analysis*

487   Figure 6.a and 6.f show land cover maps for two arbitrary 0.75°×0.75° grids within North

488   America (hereafter referred as to Sites A and B). Also shown are the enlarged 3-year time series

489   (from January 2004 to December 2006) for AMSR-E LPRM soil moisture and corresponding

490   spectral analysis within each 0.25°×0.25° grid located at the center of these 0.75°×0.75° grids –

491   as outlined by the black boxes. Both sites in Figure 6 represent highly heterogeneous land surface

492   conditions. From the GlobeLand30 land cover map of Site A (latitude: 38.875° N, longitude:

493   121.125° W), a highly heterogeneous satellite orbit overpassing region can be observed with large

494   portions of forest and urban land cover. Meanwhile, the fractions of water bodies, crop, grassland,

495   and shrubland land cover types are also non-trivial with a relatively clear spatial pattern (Figure

496   6.a). In particular, the urban area is mainly located in the lower-left corner, while forest covers

497   upper-right corner. Grassland is mixed with crop, shrubland and water bodies. A strong negative

498   trend in vegetation density from upper-right to lower-left can be observed.

499   The soil moisture time series for Site A (Figure 6.b and Figure 6.c) demonstrates a

500   relatively strong seasonal climatology with values varying from 0.01 to 0.5 (m^3/m^3). AMSR-E

501   LPRM soil moisture retrieval for each quarter degree grid is generated based as the mean of all

502   swath data whose footprint centers fall within that particular grid (Owe et al., 2008). The soil

503   moisture record manifests several significant spectral resonances – including a significant 8-day

504 peak. Moreover, 4-day and 16-day peaks are also conspicuous for both overpasses. Given their

505 uses in LPRM retrievals, the T_B-derived *MPDI* and *MWE* are also analyzed in frequency domain.

506 Similarly, an 8-day peak in *MPDI* appears in both half-orbits – suggesting that the spectral peaks

507 in soil moisture retrievals can be traced back to the *MPDI*. However, the probability of occurrence

508 and the relative amplitude of spectral peaks in soil moisture and *MPDI* are not exactly the same

509 for each peak. On the other hand, the PSDs of *MWE* also show 8-day and 4-day spectral peaks for

510 the ascending overpass (Figure 6.e) and a 4-day peak for the descending overpass (Figure 6.d).

511 Therefore, within Site A, strong spatial heterogeneity in land cover appears capable of generating

512 soil moisture spectral peaks associated with the satellite orbiting cycle.

513   Likewise, Site B (latitude: 34.125° N, longitude: 87.125° W) exhibits strong spatial land

514 cover heterogeneity (Figure 6.f). Specifically, forest covers the north-western regions and is mixed

515 with crops and grasslands. Small patches of urban and water bodies are sparsely distributed

516 throughout the scene. The soil moisture time series values range from 0.01 to 0.7 (m^3/m^3). Despite

517 a lack of strong large-scale spatial variation, this site also demonstrates heterogeneous land surface

518 characteristics with different land cover types thoroughly mixed with each other. Both the

519 ascending and descending soil moisture time series contain 8-day peaks in the frequency domain

520 (Figure 6.i and Figure 6.j) with the ascending peak more prominent. For the descending overpass,

521 the more equivalent thermodynamic conditions are beneficial for applying the LPRM soil moisture

522 retrieval algorithm. A significant 8-day peak in the descending *MPDI* does not lead to a

523 comparable peak in the soil moisture retrievals (Figure 6.i). Also, fewer peaks are observed in the

524 PSDs of *MWE* compared to Site A. Other factors such as the vegetation density and soil and canopy

525 effective temperatures in the retrieval process can play a role in determining the retrieved soil

526 moisture. Specifically, the microwave radiation emitted from water bodies is quite different from

527 other land cover types and can strongly impact in soil moisture retrievals (Gouweleeuw et al.,

528 2012).
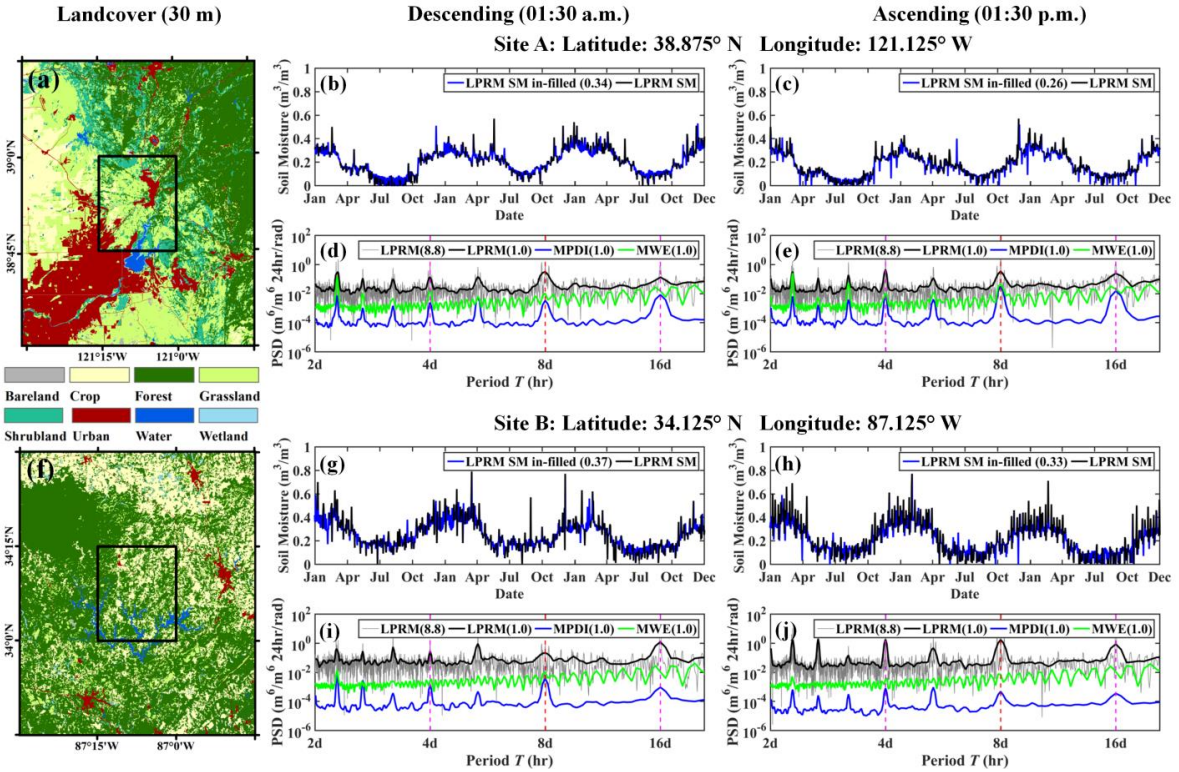
Figure 6. Site-specified demonstrations of high resolution land cover (a and f), descending (b, d, g, and i) and

531 ascending (c, e, h, and j) AMSR-E LPRM soil moisture and brightness temperature (T_B). Each land cover map depicts

532 a 0.75°×0.75° grid centered at different locations (Sites A and B) with the black box outlines the 0.25°×0.25° grid.

533 Maps are projected in WGS 1984 UTM coordinate system and latitudes and longitudes of sites are shown as well.

534 Enlargements of the 3-years (from January 2004 to December 2006) time series of soil moisture retrievals are included

535 for each site and the infilling fractions are shown in the brackets. The spectral analyses are conducted for AMSR-E

536 LPRM soil moisture retrievals and T_B-derived Microwave Polarization Difference Index (*MPDI*) and Microwave

537 Emissivity (*MWE*). The Hamming window sizes for PSD estimations are indicated by units of year in the brackets.

538 Dotted vertical lines represent three periods at 4-day, 8-day, and 16-day.

539   In contrast to the relatively heterogeneous sites examined in Figure 6, Figure 7 looks at two

540 spatially homogeneous sites (Sites C and D). The two sites are dominated by grassland and crop

541 cover, respectively. The coverage fractions of other land cover types are relatively negligible. Both

542   soil moisture time series depict a relatively small seasonal climatology compared to Figure 6

543   without the orbiting cycle-related spectral peaks. Also, no prominent peaks are observed from the

544   PSDs of both T_B-derived *MPDI* and *MWE*.
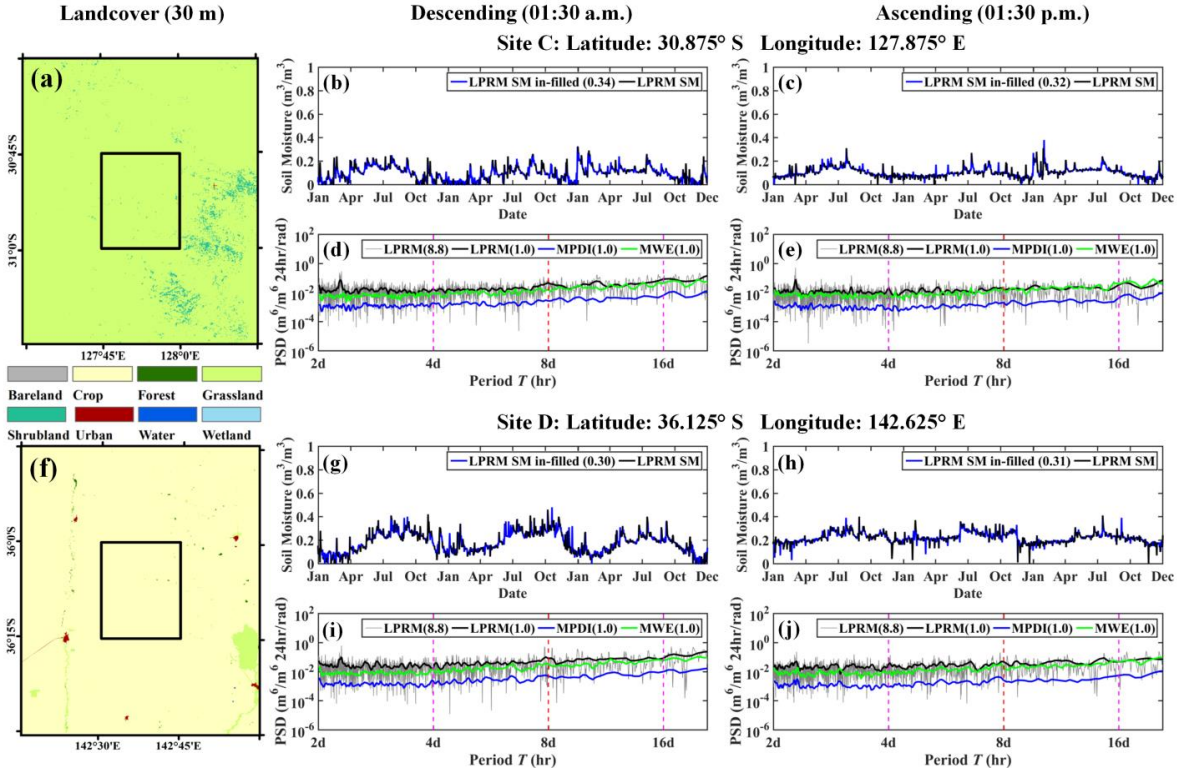
546   **Figure 7.** Same with Figure 6 except for Sites C and D.

547   By investigating four different sites with various spatial coverages of land cover types, a

548   possible link between spectral peaks of retrieved soil moisture and the directly observed T_B can be

549   inferred. The spatial heterogeneity combined with systematic orbiting cycle can lead to the spectral

550   peaks in *MPDI* and thus soil moisture retrievals.

551

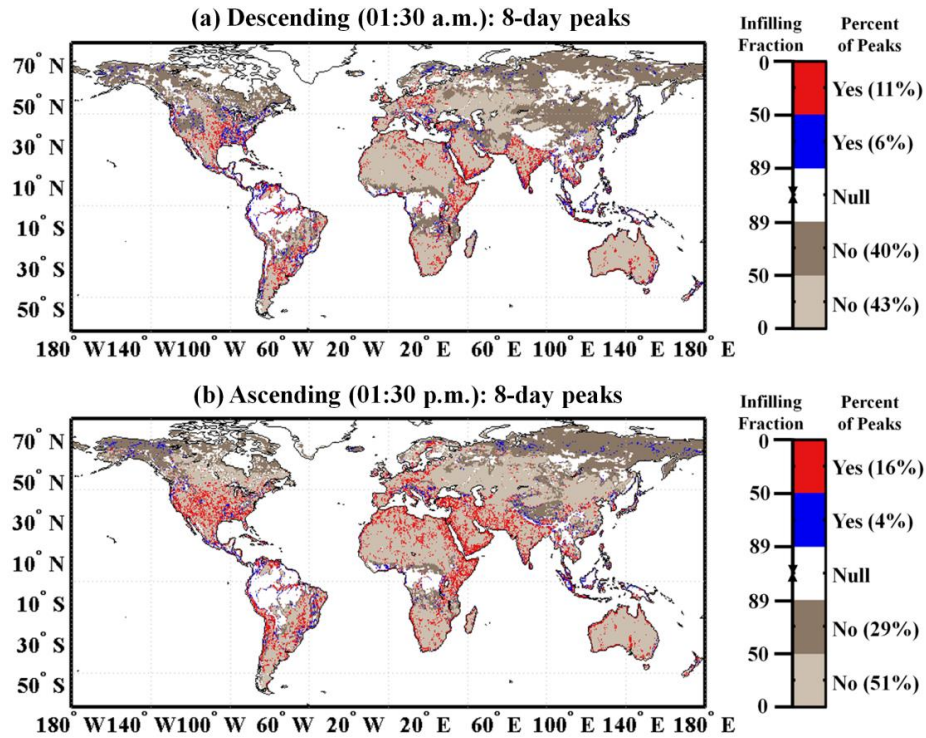552   *3.3. Global distribution of spectral peaks*

553   While interesting, results in Figures 6 and 7 are clearly anecdotal in nature. In order to

554   examine more general tendencies, global distributions of the 8-day spectral peaks in LPRM

555   AMSR-E soil moisture retrievals are plotted in Figure 8 for both descending and ascending

556   overpasses. Regions with high (over 50%) infilling fractions (Figure 1.c and 1.d) are indicated

557   with different color settings for grids with or without 8-day spectral peaks.

558   Generally speaking, the spatial distribution of spectral peaks is similar for both half-orbits.

559   However, relatively more peaks are found in the ascending half-orbit – 20% versus 17% of the

560   total grids over the globe. Both descending and ascending overpasses have demonstrated notable

561   spectral peaks over densely-vegetated areas of Eastern CONUS. On the other hand, there exist

562   moderately different distributions of peaks over Western CONUS. Note that significant

563   discrepancies of near-surface (soil, canopy and air) vertically thermal profiles can be observed

564   between the AMSR-E nighttime descending (01:30 a.m.) and daytime ascending (01:30 p.m.)

565   overpasses. During nighttime, near-surface isothermal conditions benefit the retrieval of soil

566   moisture from brightness temperature observations with higher accuracy (Jackson et al., 2010),

567   yielding less spurious spectral peaks in the descending overpass.

568   Comparing regions with high infilling fractions (blue and dark brown in Figure 8) against

569   other grids (red and light brown), the probability of identified peaks can be lower with 12% (4/33)

570   versus 24%, and 13% versus 20% for ascending and descending overpasses, respectively. With

571   increased infilling fractions, more in-filled data are included for the peak detection, which may

572   lead to possible missed identification of peaks (please refer to section A of the supporting materials

573   for more details). Nevertheless, as our gap-filling approach does not lead to occurrence of peaks,

574   any peaks detected for grids with high infilling fraction should be prominent and therefore are

575   preserved for the global distribution mapping.

576   Additionally, comparing Figure 8 and Figure 1.a or Figure 1.b, the presence of RFI may

577   impact the occurrence of spectral peaks. See section 4.1 for additional discussion on this point.

28

Figure 8. Global distribution maps of 8-day spectral peaks in the AMSR-E LPRM soil moisture product for both (a) descending and (b) ascending half-orbits. Regions with in-filled data over (below) 50% are shown in dark (light) brown. Accordingly, grids with peaks are demonstrated in blue or red color. Percentages of grids with/without 8-day peaks in regard to the total grids for both descending and ascending overpasses are computed, respectively.

Furthermore, the global spectral analyses are conducted for the T_B-derived *MPDI* and *MWE* as shown in Figure 9. As depicted, both descending (Figure 9.a and 9.c) and ascending (Figure 9.b and 9.d) half-orbits have a similar spatial distribution pattern with regard to *MPDI* or *MWE*. Overall spatial patterns of 8-day peaks in *MPDI* are comparable with that in soil moisture retrievals. However, 8-day peaks in *MPDI* are relatively more common than soil moisture peaks in Figure 8. Comparing to (relatively dynamic) soil moisture values, *MPDI* is more likely to respond to temporally-stable land surface elements, such as land cover type and vegetation density.
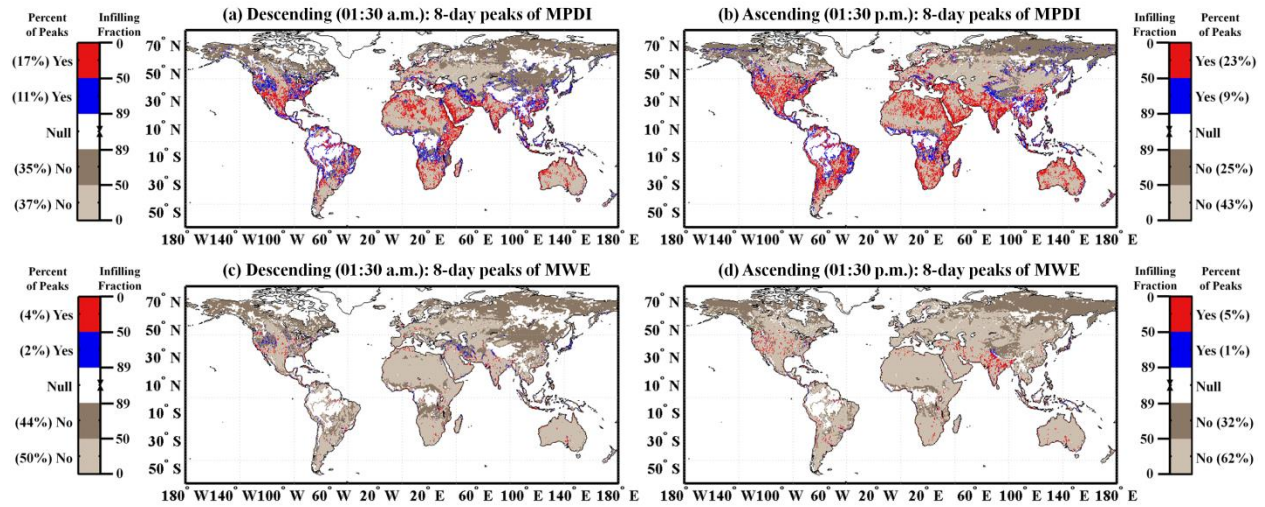
Figure 9. Global distribution maps of 8-day spectral peaks in AMSR-E -derived *MPDI* (a and b) and *MWE* (c and d) for both descending and ascending half-orbits. Color setting is same as Figure 8 and percentages of grids with/without 8-day peaks are also shown in the legend.

In contrast, *MWE* maps demonstrate relatively fewer peaks than soil moisture in Figure 8. *MWE* as a function of several varying variables, including water content and soil salinity, changes rapidly over land surface (Prigent et al., 2006). More specifically, the intensity and duration of precipitation events modulate the land surface emissivity (Ferraro et al., 2013). Consequently, *MWE* does not generally show strong and persistent land surface heterogeneity over the 16-day exact repeat cycle of AMSR-E sensor. Taken as a whole, Figure 9 suggests a primary role for *MPDI* as the source of periodicity in LPRM soil moisture retrievals.

3.4. Relating the 8-day periodic error to spatial heterogeneity

To explore the relationship between the presence of an 8-day spectral peak in soil moisture retrievals and the land surface spatial heterogeneity, three heterogeneity indicators are computed for each quarter degree grid (see section 2.4 above). Figure 10 shows global maps of these three heterogeneity indicators, namely TB-HI, VI-HI, and LC-HI. For each map, larger values indicate

607 larger amounts of land surface spatial heterogeneity although the valid ranges are different for each

608 indicator (see Table 1 for details).

609
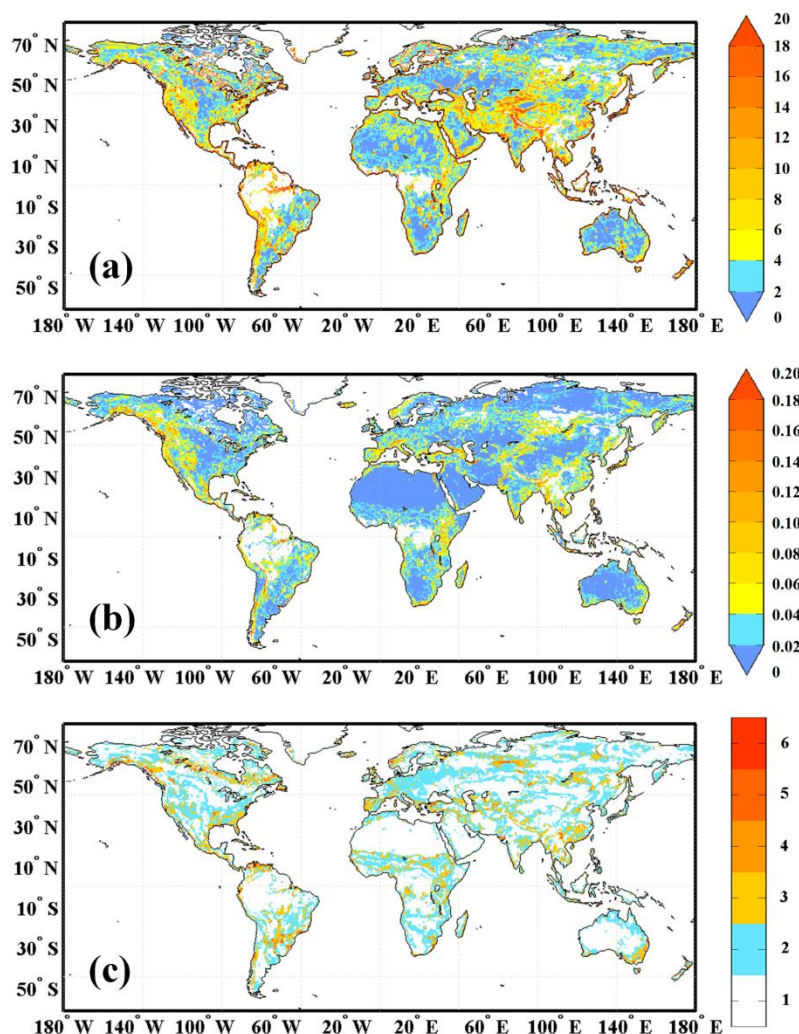
Figure 10. Global maps of three heterogeneity indicators calculated from: (a) AMSR-E T_B observations, (b) long-term averaged vegetation index and (c) land cover types.

612 The three maps show different aspects of spatial heterogeneity which results in different

613 distributions of indicator values. Nevertheless, the spatial distribution of high heterogeneity

614 indicators is generally consistent with the occurrence of 8-day peaks in the AMSR-E LPRM soil

615 moisture product (Figure 8). Regions such as the Amazon and the Tibetan Plateau have

616 demonstrated a significant relationship that grids with 8-day peaks have extremely high TB-HI

617   (Figure 10.a). Likewise, in western CONUS, South America, South Africa, and India, a relatively

618   close link can be observed. Along the west coast of South America and over West Central Africa,

619   a comparable distribution of high VI-HI and grids with 8-day peak is observable (Figure 10.b).

620   LC-HI also shows some high values for central Southern Africa (Figure 10.c) where 8-day peaks

621   are frequently detected.

622   Both VI-HI and LC-HI fail to capture the information over non-vegetated landscapes, e.g.,

623   North Africa and the Arabian Peninsula. These two indicators are based solely on relatively coarse-

624   resolution land cover characteristics and cannot fully represent the land surface variability. Instead,

625   other factors not captured in the indices, such as soil texture and roughness, may play a primary

626   role in determining the heterogeneity for low-vegetated regions.

627   Table 1 shows the global mean and median values for each of the three indicators, both for

628   grids with and without 8-day peaks. Under all circumstances, grids with the 8-day peak are

629   associated with relative higher mean and median values of the heterogeneity indicators. This

630   further suggests that the occurrence of spectral peaks can be related to the land surface spatial

631   heterogeneity. In addition, Figure 11 shows the normalized histograms (to [0,100]) of three

632   indicators over the globe for grids with or without 8-day peaks. Descending and ascending

633   overpasses are separately processed and the statistical hypothesis test (Wilcoxon-Mann-Whitney

634   test) has been performed for six scenarios. All test results indicate that the median of the indicator

635   for grids with peaks is greater than that for grids without peaks at a 0.001 significance level. This

636   suggests a statistically significant capability for the three heterogeneity indicators to characterize

637   regions with strong land surface variability.

638   **Table 1.** Global means and medians of three heterogeneity indicators under two conditions: with or without 8-day

639   peaks identified in soil moisture retrievals. Statistics for both descending (01:30 a.m.) and ascending (01:30 p.m.)

640   half-orbits are calculated. Data in parentheses are computed for regions with infilling fraction smaller than 50%.

Indicator	Descending		Ascending		Valid Range
	Yes	No	Yes	No	
Mean					
TB-HI	15.30 (13.01)	5.70 (4.89)	12.98 (11.45)	6.18 (4.91)	[0 100]
VI-HI	0.06 (0.05)	0.03 (0.03)	0.05 (0.05)	0.03 (0.03)	[0 0.4]
LC-HI	2.09 (2.07)	1.66 (1.62)	1.97 (1.94)	1.70 (1.63)	[1 6]
Median					
TB-HI	7.29 (6.91)	3.20 (3.09)	6.38 (6.21)	3.22 (3.01)	[0 100]
VI-HI	0.04 (0.04)	0.02 (0.02)	0.03 (0.03)	0.02 (0.02)	[0 0.4]
LC-HI	2 (2)	1 (1)	2 (2)	2 (1)	[1 6]

For grid cells without peaks, nearly half has the lowest level of spatial heterogeneity indicators. For example, 61.54% (61.00%) of grids without peaks in descending (ascending) overpass has a TB-HI smaller than 4 (Figure 11.a and 11.b). Conversely, over 74% (71%) of grids with peaks in descending (ascending) overpass has a TB-HI larger than 4. Similar contrasts can be found for the other indicators. Overall, grids with higher values of the heterogeneity indicators are more likely to contain 8-day peaks in soil moisture retrievals.
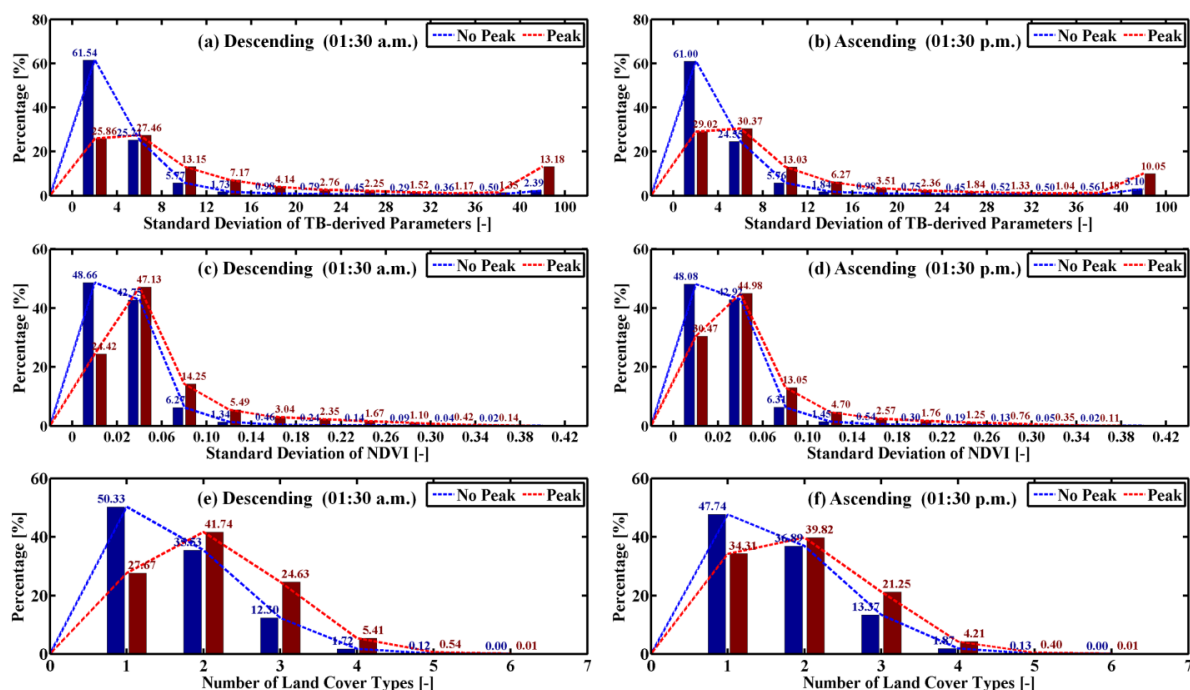
Figure 11. Histograms of three heterogeneity indicators for grids with or without 8-day peaks. Descending and ascending overpasses are separately processed over the globe.

IV. Discussion

The accurate characterization of errors in remotely sensed soil moisture products is important for satellite calibration/validation activities and the development of optimized assimilation approach for integrating retrievals with hydrologic modeling. In contrast to the common assumption of temporally white errors, Su et al. (2013a) demonstrated that AMSR-E and SMOS gridded soil moisture products over Australia depict spectral resonances suggesting the existence of periodic errors. Here, we expanded the time series spectral analysis in Su et al. (2013a) to a global domain and explored the physical origins of these periodic errors.

Through the synthetic experiments, the periodic errors can be linked to the combination of the periodic sampling patterns and the land surface spatial heterogeneity (Figure 5). Results of AMSR-E LPRM soil moisture product further presented a link of spectral peaks existing in T_B-derived *MPDI* and soil moisture retrievals. More specifically, that spatial heterogeneity within the satellite's field-of-view can lead to the periodicity in *MPDI* estimates which are then transmitted into soil moisture retrievals. As demonstrated in Figure 8, LPRM soil moisture derived from both ascending and descending overpasses demonstrate significant 8-day spectral peaks along coastal areas and some regions with water bodies, e.g., the Amazon floodplain and areas of central Australia with ephemeral salt lakes. In addition, regions with spatially-heterogeneous land cover (e.g., eastern CONUS, South America, Western Europe, Peninsular India, and southern China) appear more likely to have the 8-day peaks.

672 *4.1. Potential role of radio frequency interference*

673   The AMSR-E LPRM soil moisture product is a combined product which has utilized both

674 C- and X-band T_B to retrieve soil moisture. The C-band frequency, which is theoretically more

675 sensitive to variations in soil moisture, is treated as the primary data source. However, over regions

676 with high RFI contaminations, the retrieval method switches from C- to X-band (shown in Figure

677 1.a and 1.b). This strategy can largely mitigate the influence of strong and spatio-temporally

678 constant RFI. Figure 6 shows an illustration of RFI impact at two heterogeneous sites with

679 contrasting land surface characteristics. For Site A, urban area covers a large portion of the

680 $0.75°×0.75°$ grid and only X-band T_B has been utilized for retrieving soil moisture. While the RFI

681 impact has been eliminated to a great extent, spectral peaks are detected from the corresponding

682 soil moisture retrievals (Figure 6.d and 6.e). In contrast, without significant RFI at Site B, C-band

683 T_B has been applied and periodic errors still exist (as shown in Figure 6.i and 6.j). This suggests

684 that the periodicity found in AMSR-E LPRM soil moisture product cannot be fully attributed to

685 RFI alone.

686   On the other hand, in addition to the T_B-derived heterogeneity indicators, another two

687 indicators which are computed from independent MODIS vegetation index and land cover type

688 information will not reflect RFI information. As depicted in Figure 11, VI-HI and LC-HI have

689 demonstrated statistically significant skills in characterizing land surface heterogeneity. Via a pre-

690 defined threshold for each heterogeneity indicator, VI-HI and LC-HI can partially differentiate

691 grids with peaks from those without peaks indicating the causal relationship between spatial

692 variability of natural land surface and the occurrence of peaks.

693   Nevertheless, similarities between RFI map (Figure 7.a in Njoku et al., 2005) and

694 ascending spectral peak map (Figure 8.b) can be observed, for example over CONUS and the

695 western Arabian Peninsula. Note that the RFI detection method is based on the spectral difference

696 between the 6.9- and 10.7 GHz channels and a threshold should be assigned to determine whether

697 RFI exists or not (Li et al., 2004). Consequently, if RFI is of low-level or spatially/temporally

698 intermittent (which is often the real case), it might escape the detection. Moreover, regions with

699 RFI contaminations are often close to urban areas, where transitions in architecture and building

700 density, vegetation, and anthropogenic activity are thoroughly mixed (Cadenasso et al., 2007).

701 Under such circumstance, a high heterogeneity of land surface characteristics (including both

702 natural and artificial features) can be observed over these regions and thus lead to more spectral

703 peaks in soil moisture retrievals. Therefore, RFI can intensify the land surface heterogeneity and

704 increase the probability of occurrence of spectral peaks in satellite-derived soil moisture retrievals.

705

706 *4.2. Impact of the infilling method*

707   To conduct the spectral analysis, the 1-D infilling method was performed to achieve

708 evenly-spaced observations. Given that the infilling method is based on statistics sampled from

709 the entire time series, the results retain the autocorrelation structure of soil moisture in the high

710 frequency domain but in-filled values are smoothed with low frequency climatology for significant

711 gaps (Wang et al., 2012). Comparing Figure 1.c or 1.d with Figure 8, no obvious spatial correlation

712 between the infilling fraction and existence of 8-day peak can be observed – suggesting that our

713 infilling approach does not lead to the spurious production of spectral peaks. Aside from high

714 latitudes near the pole where the interpolation fraction is extremely large and there is less chance

715 of having 8-day peaks, in most regions with small infilling fractions, such as Western Europe,

716 South America, Africa, and Australia, there is no evidence that the gap infilling has an impact on

717 the frequency of peak occurrence.

718   In order to further examine this point, a synthetic control test has been conducted to explore

719   the impact of infilling fraction. Details can refer to section A in the supporting materials. The

720   results demonstrated that, as expected, the accuracy of in-filled soil moisture time series gradually

721   decreases with increasing infilling fractions. However, no spurious spectral peaks will be

722   introduced by the infilling method, suggesting that any spectral peaks detected in the in-filled soil

723   moisture data are present in the original time series. Further studies may explore alternative PSD

724   estimation approaches (such as the Lomb-Scargle periodogram (Lomb, 1976; Scargl, 1982) or

725   wavelet transform-based method (Foster, 1996) which do not require evenly-spaced observations.

726

727   *4.3. Potential applications*

728   Results in Figure 8 identified significant periodic error components in existing soil

729   moisture remote sensing product and globally mapped their distribution. Removing such

730   systematic error components is a critical goal of satellite calibration activities and could potentially

731   aid in the development of optimized gridding and processing procedures. A global identification

732   map of such periodic errors would also be beneficial for identifying highly heterogeneous regions

733   for the targeted application of a band-stop filter (Su et al., 2013a; 2015) for removing the

734   systematic periodic errors in short-term satellite-derived soil moisture products.

735   For short-term available satellite-based soil moisture products, the baseline of applying the

736   band-stop filtering is to apply it indiscriminately to every grid cell. In this case, the majority of

737   grids without significant frequency peaks can be over-smoothed (because over 80% of global grid

738   cells lack 8-day soil moisture peaks). Moreover, spatial heterogeneity may similarly affect other

739   satellite-based products, particularly when they have similar orbital configurations and retrieval

740   inputs as AMSR-E LPRM. For satellite records which are too short for PSD estimation, one option

741   is to utilize a peak distribution map generated from the long-term (9+ year) AMSR-E soil moisture

742   time series as the criterion for identifying heterogeneous regions in which to apply a band-stop

743   filter.

744

745   **V. Conclusions**

746   Via a synthetic experiment imitating the periodic sampling pattern of polar-orbiting

747   satellite swaths over various land cover characteristics, the combination of spatial land surface

748   heterogeneity and periodic orbital sampling pattern are linked to periodic errors in remotely-sensed

749   soil moisture retrievals (Figure 5). In data real cases utilizing AMSR-E LPRM soil moisture

750   retrievals, site-specific studies demonstrate that the satellite repeat cycle can generate a periodicity

751   in the T_B-derived *MPDI* and corresponding LPRM soil moisture retrievals (Figures 6 and 7). By

752   applying the peak detection method, global distribution maps of 8-day peaks in AMSR-E LPRM

753   soil moisture retrievals and T_B-derived *MPDI* and *MWE* can be generated. Comparisons between

754   these maps show strong evidence that the satellite orbiting cycle-related spectral peaks are more

755   likely to occur in highly-heterogeneous land regions (Figures 8 and 9). The conclusion is intuitive

756   to understand. The re-gridding method of satellite observations is usually based on a selection of

757   all footprints within the same orbital overpass covering the given grid. Due to the progression of

758   the satellite orbit, the track changes from day to day with an exact repeat cycle and thus introduces

759   the periodic errors into the sampling over regions with large land surface heterogeneity.

760   The global identification of the periodic error is of importance for the data assimilation

761   community and will also support the development of improved soil moisture re-gridding and post-

762   processing methods. To globally correlate the occurrence of such spectral peaks with heterogeneity

763   in land surface characteristics, three heterogeneity indicators have been proposed and shown their

764 statistically significant capability in detecting high-heterogeneous regions with 8-day peaks

765 (Figure 10, Figure 11, and Table 1). The association between heterogeneity indicators and the

766 occurrence of 8-day periodic errors is compelling evidence of the causal link between land surface

767 spatial heterogeneity and the periodic errors in satellite-based re-gridded soil moisture product.

768 While these heterogeneity indicators have demonstrated statistically significant skills at a

769 global scale, they do not predict all peaks (and predict some peaks which to not occur). As a result,

770 further refinement of these indicators is necessary to make them of immediate value in an

771 operational retrieval and/or data assimilation context. Nevertheless, results presented here

772 represent an important first step in this direction as both synthetic and real data results provide

773 clear evidence of a general link between land surface spatial heterogeneity and the occurrence of

774 periodic errors in AMSR-E soil moisture retrievals. Additionally, other PSD estimation approaches

775 and soil moisture products using different retrieval algorithms (Kim et al., 2015), such as the JAXA

776 product retrieved by Japan Aerospace Exploration Agency, should be included in follow-on

777 analyses.

778

779 **Acknowledgement**

787

References

789   Al-Yaari, A., J. P. Wigneron, A. Ducharne, Y. Kerr, P. De Rosnay, R. De Jeu, A. Govind, A. Al Bitar, C. Albergel,
790   and J. Munoz-Sabater (2014), Global-scale evaluation of two satellite-based passive microwave soil moisture
791   datasets (SMOS and AMSR-E) with respect to Land Data Assimilation System estimates, Remote Sensing of
792   Environment, 149, 181-195.
793   Alvarez-Garreton, C., D. Ryu, A. Western, W. Crow, and D. Robertson (2014), The impacts of assimilating satellite
794   soil moisture into a rainfall–runoff model in a semi-arid catchment, Journal of Hydrology, 519, 2763-2774.
795   Bolten, J. D., W. T. Crow, X. Zhan, T. J. Jackson, and C. A. Reynolds (2010), Evaluating the utility of remotely sensed
796   soil moisture retrievals for operational agricultural drought monitoring, IEEE Journal of Selected Topics in
797   Applied Earth Observations and Remote Sensing, 3(1), 57-66.
798   Brocca, L., S. Hasenauer, T. Lacava, F. Melone, T. Moramarco, W. Wagner, W. Dorigo, P. Matgen, J. Martínez-
799   Fernández, and P. Llorens (2011), Soil moisture estimation through ASCAT and AMSR-E sensors: An
800   intercomparison and validation study across Europe, Remote Sensing of Environment, 115(12), 3390-3408.
801   Brovelli, M. A., M. E. Molinari, E. Hussein, J. Chen, and R. Li (2015), The first comprehensive accuracy assessment
802   of GlobeLand30 at a national level: methodology and results, Remote Sensing, 7(4), 4191-4212.
803   Burgers, G., P. Jan van Leeuwen, and G. Evensen (1998), Analysis scheme in the ensemble Kalman filter, Monthly
804   Weather Review, 126(6), 1719-1724.
805   Cadenasso, M. L., S. T. Pickett, and K. Schwarz (2007), Spatial heterogeneity in urban ecosystems: reconceptualizing
806   land cover and a framework for classification. Frontiers in Ecology and the Environment, 5(2), 80-88.
807   Chan, S., E. Njoku, and A. Colliander (2012), SMAP Algorithm Theoretical Basis Document: L1C Radiometer Data
808   Product, Tech. Rep. SMAP Project, JPL D-53053, Jet Propulsion Laboratory, Pasadena, CA.
809   Chen, J., J. Chen, A. Liao, X. Cao, L. Chen, X. Chen, C. He, G. Han, S. Peng, and M. Lu (2015), Global land cover
810   mapping at 30m resolution: A POK-based operational approach, ISPRS Journal of Photogrammetry and Remote
811   Sensing, 103, 7-27.
812   Chen, S. S., X. Z. Chen, W. Q. Chen, Y. X. Su, and D. Li (2011), A simple retrieval method of land surface temperature
813   from AMSR-E passive microwave data—A case study over Southern China during the strong snow disaster of
814   2008. International Journal of Applied Earth Observation and Geoinformation, 13(1), 140-151.
815   Crow, W. T., and M. Van den Berg (2010), An improved approach for estimating observation and model error
816   parameters in soil moisture data assimilation, Water Resources Research, 46(12), W12519.
817   Crow, W. T., and X. Zhan (2007), Continental-scale evaluation of remotely sensed soil moisture products, IEEE
818   Geoscience and Remote Sensing Letters, 4(3), 451-455.
819   Crow, W. T., G. J. Huffman, R. Bindlish, and T. J. Jackson (2009), Improving satellite-based rainfall accumulation
820   estimates using spaceborne surface soil moisture retrievals, Journal of Hydrometeorology, 10(1), 199-212.

821   Daganzo-Eusebio, E., R. Oliva, Y. H. Kerr, S. Nieto, P. Richaume, and S. M. Mecklenburg (2013), SMOS radiometer
822   in the 1400–1427-MHz passive band: Impact of the RFI environment and approach to its mitigation and
823   cancellation, IEEE Transactions on Geoscience and Remote Sensing, 51(10), 4999-5007.

824   De Jeu, R. A. M. and M. Owe (2003), Further validation of a new methodology for surface moisture and vegetation
825   optical depth retrieval, International Journal of Remote Sensing, 24(22), 4559-4578.

826   De Jeu, R., W. Wagner, T. Holmes, A. Dolman, N. Van De Giesen, and J. Friesen (2008), Global soil moisture patterns
827   observed by space borne microwave radiometers and scatterometers, Surveys in Geophysics, 29(4), 399-420.

828   De Jeu, R. A., T. R. Holmes, R. Panciera, and J. P. Walker (2009), Parameterization of the land parameter retrieval
829   model for L-band observations using the NAFE'05 data set, IEEE Geoscience and Remote Sensing Letters, 6(4),
830   630-634.

831   Dorigo, W. A., A. Gruber, R. A. M. De Jeu, W. Wagner, T. Stacke, A. Loew, C. Albergel, L. Brocca, D. Chung, R.
832   M. Parinussa, and R. Kidd (2015), Evaluation of the ESA CCI soil moisture product using ground-based
833   observations. Remote Sensing of Environment, 162, 380-395.

834   Dorigo, W. A., A. Xaver, M. Vreugdenhil, A. Gruber, A. Hegyiová, A. D. Sanchis-Dufau, D. Zamojski, C. Cordes,
835   W. Wagner, and M. Drusch (2013), Global automated quality control of in situ soil moisture data from the
836   International Soil Moisture Network, Vadose Zone Journal, 12(3), vzj2012-0097.

837   Dorigo, W., K. Scipal, R. Parinussa, Y. Liu, W. Wagner, R. De Jeu, and V. Naeimi (2010), Error characterisation of
838   global active and passive microwave soil moisture datasets, Hydrology and Earth System Sciences, 14(12), 2605-
839   2616.

840   Dorigo, W., W. Wagner, R. Hohensinn, S. Hahn, C. Paulik, A. Xaver, A. Gruber, M. Drusch, S. Mecklenburg, and P.
841   v. Oevelen (2011), The International Soil Moisture Network: a data hosting facility for global in situ soil moisture
842   measurements, Hydrology and Earth System Sciences, 15(5), 1675-1698.

843   Draper, C., J. Walker, P. Steinle, R. De Jeu, and T. Holmes (2009), An evaluation of AMSR-E derived soil moisture
844   over Australia, Remote Sensing of Environment, 113(4), 703-710.

845   Draper, C. S., R. H. Reichle, G. J. M. De Lannoy, and Q. Liu (2012), Assimilation of passive and active microwave
846   soil moisture retrievals, Geophysical Research Letters, 39(4), L04401.

847   Du, J. (2012), A method to improve satellite soil moisture retrievals based on Fourier analysis, Geophysical Research
848   Letters, 39(15), L15404.

849   Engman, E. T. (1991), Applications of microwave remote sensing of soil moisture for water resources and agriculture,
850   Remote Sensing of Environment, 35(2), 213-226.

851   Entin, J. K., A. Robock, K. Y. Vinnikov, S. E. Hollinger, S. Liu, and A. Namkhai (2000), Temporal and spatial scales
852   of observed soil moisture variations in the extratropics, Journal of Geophysical Research, 105(D9), 11865-11877.

853   Ferraro, R. R., C. D. Peters-Lidard, C. Hernandez, F. J. Turk, F. Aires, C. Prigent, X. Lin, S. A. Boukabara, F. A.
854   Furuzawa, K. Gopalan, and K. W. Harrison (2013), An evaluation of microwave land surface emissivities over
855   the continental United States to benefit GPM-era precipitation algorithms. IEEE Transactions on Geoscience and
856   Remote Sensing, 51(1), 378-398.

857   Foster, G (1996), Wavelets for period analysis of unevenly sampled time series, The Astronomical Journal, 112(4),
858   1709-1729.

859   Garcia, D. (2010), Robust smoothing of gridded data in one and higher dimensions with missing values,
860   Computational Statistics and Data Analysis, 54(4), 1167-1178.

861   Gouweleeuw, B., A. van Dijk, J. P. Guerschman, P. Dyce, and M. Owe (2012), Space-based passive microwave soil
862   moisture retrievals and the correction for a dynamic open water fraction, Hydrology and Earth System Sciences,
863   16(6), 1635-1645.

864   Grody, N. C. (1993), Remote sensing of the atmosphere from satellites using microwave radiometry. In Atmospheric
865   remote sensing by microwave radiometry, Editor: Michael A. Janssen, 259-334.

866   Gruber, A., W. Dorigo, S. Zwieback, A. Xaver, and W. Wagner (2013), Characterizing coarse-scale representativeness
867   of in situ soil moisture measurements from the International Soil Moisture Network, Vadose Zone Journal, 12(2):
868   vzj2012-0170.

869   Holmes, T. R. H., W. T. Crow, C. Hain, M. C. Anderson, and W. P. Kustas (2015), Diurnal temperature cycle as
870   observed by thermal infrared and microwave radiometers. Remote Sensing of Environment, 158, 110-125.

871   Holmes, T., R. De Jeu, M. Owe, and A. Dolman (2009), Land surface temperature from Ka band (37 GHz) passive
872   microwave observations, Journal of Geophysical Research: Atmospheres, 114, D04113.

873   Jackson, T. J., T. J. Schmugge, and J. R. Wang (1982), Passive microwave sensing of soil moisture under vegetation
874   canopies. Water Resources Research, 18(4), 1137-1142.

875   Jackson, T. J., M. H. Cosh, R. Bindlish, P. J. Starks, D. D. Bosch, M. Seyfried, D. C. Goodrich, M. S. Moran, and J.
876   Du (2010), Validation of advanced microwave scanning radiometer soil moisture products, IEEE Transactions
877   on Geoscience and Remote Sensing, 48(12), 4256-4272.

878   Katul, G. G., A. Porporato, E. Daly, A. C. Oishi, H. S. Kim, P. C. Stoy, J. Y. Juang, and M. B. Siqueira (2007), On
879   the spectrum of soil moisture from hourly to interannual scales, Water Resources Research, 43(5), 1-10.

880   Kim, S., Y. Liu, F. M. Johnson, R. M. Parinussa, and A. Sharma (2015), A global comparison of alternate AMSR2
881   soil moisture products: Why do they differ?, Remote Sensing Environment, 161, 43-62.

882   Komma, J., G. Blöschl, and C. Reszler (2008), Soil moisture updating by Ensemble Kalman Filtering in real-time
883   flood forecasting, Journal of Hydrology, 357(3), 228-242.

884   Koster, R. D., P. A. Dirmeyer, Z. Guo, G. Bonan, E. Chan, P. Cox, C. Gordon, S. Kanae, E. Kowalczyk, and D.
885   Lawrence (2004), Regions of strong coupling between soil moisture and precipitation, Science, 305(5687), 1138-
886   1140.

887   Lacava, T., V. Cuomo, E. V. Di Leo, N. Pergola, F. Romano, and V. Tramutoli (2005), Improving soil wetness
888   variations monitoring from passive microwave satellite data: the case of April 2000 Hungary flood, Remote
889   Sensing of Environment, 96(2), 135-148.

890   Lakhankar, T., N. Krakauer, and R. Khanbilvardi (2009a), Applications of microwave remote sensing of soil moisture
891   for agricultural applications, International Journal of Terraspace Science and Engineering, 2(1), 81-91.

892   Lakhankar, T., H. Ghedira, M. Temimi, A. E. Azar, and R. Khanbilvardi (2009b), Effect of land cover heterogeneity
893   on soil moisture retrieval using active microwave remote sensing data. Remote Sensing, 1(2), 80-91.

894   Li, L., E. G. Njoku, E. Im, P. S. Chang, and K. S. Germain (2004), A preliminary survey of radio-frequency
895   interference over the US in Aqua AMSR-E data, IEEE Transactions on Geoscience and Remote Sensing, 42(2),
896   380-390.

897   Lin, B., B. Wielicki, P. Minnis, and W. Rossow (1998), Estimation of water cloud properties from satellite microwave,
898   infrared and visible measurements in oceanic environments: 1. Microwave brightness temperature simulations.
899   Journal of Geophysical Research: Atmospheres, 103(D4), 3873-3886.

900   Loew, A. (2008), Impact of surface heterogeneity on surface soil moisture retrievals from passive microwave data at
901   the regional scale: The Upper Danube case. Remote Sensing of Environment, 112(1), 231-248.

902   Lomb, N. R. (1976), Least-squares frequency analysis of unequally spaced data, Astrophysics and Space Science,
903   39(2), 447-462.

904   Meesters, A. G., R. A. De Jeu, and M. Owe (2005), Analytical derivation of the vegetation optical depth from the
905   microwave polarization difference index, IEEE Geoscience and Remote Sensing Letters, 2(2), 121-123.

906   Mo, T., B. Choudhury, T. Schmugge, J. Wang, and T. Jackson (1982), A model for microwave emission from
907   vegetation−covered fields, Journal of Geophysical Research: Oceans, 87(C13), 11229-11237.

908   Moody, A., and D. M. Johnson (2001), Land-surface phenologies from AVHRR using the discrete Fourier transform,
909   Remote Sensing of Environment, 75(3), 305-323.

910   Njoku, E. G., T. J. Jackson, V. Lakshmi, T. K. Chan, and S. V. Nghiem (2003), Soil moisture retrieval from AMSR-
911   E, IEEE Transactions on Geoscience and Remote Sensing, 41(2), 215-229.

912   Njoku, E. G., P. Ashcroft, T. K. Chan, and L. Li (2005), Global survey and statistics of radio-frequency interference
913   in AMSR-E land observations, IEEE Transactions on Geoscience and Remote Sensing, 43(5), 938-947.

914   Owe, M., R. de Jeu, and J. Walker (2001), A methodology for surface soil moisture and vegetation optical depth
915   retrieval using the microwave polarization difference index, IEEE Transactions on Geoscience and Remote
916   Sensing, 39(8), 1643-1654.

917   Owe, M., R. de Jeu, and T. Holmes (2008), Multisensor historical climatology of satellite-derived global land surface
918   moisture, Journal of Geophysical Research: Earth Surface (2003-2012), 113, F01002.

919   Parinussa, R. M., A. G. C. A. Meesters, Y. Liu, W. Dorigo, W. Wagner, and R. A. M. De Jeu (2011), Error estimates
920   for near-real-time satellite soil moisture as derived from the land parameter retrieval model, Geoscience and
921   Remote Sensing Letters, IEEE, 8(4), 779-783.

922   Prigent, C., F. Aires, and W. B. Rossow (2006), Land surface microwave emissivities over the globe for a decade.
923   Bulletin of the American Meteorological Society, 87(11), 1573-1584.

924   Rebel, K., R. De Jeu, P. Ciais, N. Viovy, S. Piao, G. Kiely, and A. Dolman (2012), A global analysis of soil moisture
925   derived from satellite observations and a land surface model, Hydrology and Earth System Sciences, 16, 833-
926   847.

927   Reichle, R. H., and R. D. Koster (2005), Global assimilation of satellite surface soil moisture retrievals into the NASA
928   Catchment land surface model, Geophysical Research Letters, 32(2), L02404.

929 Reichle, R. H., R. D. Koster, J. Dong, and A. A. Berg (2004), Global soil moisture from satellite observations, land
930   surface models, and ground data: Implications for data assimilation, Journal of Hydrometeorology, 5(3), 430-
931   442.

932 Reichle, R. H., R. D. Koster, P. Liu, S. P. Mahanama, E. G. Njoku, and M. Owe (2007), Comparison and assimilation
933   of global soil moisture retrievals from the Advanced Microwave Scanning Radiometer for the Earth Observing
934   System (AMSR-E) and the Scanning Multichannel Microwave Radiometer (SMMR), Journal of Geophysical
935   Research: Atmospheres, 112(D9), 9108.

936 Scargle, J. D. (1982), Studies in astronomical time series analysis. II-Statistical aspects of spectral analysis of unevenly
937   spaced data, The Astrophysical Journal, 263, 835-853.

938 Scharlemann, J. P., D. Benz, S. I. Hay, B. V. Purse, A. J. Tatem, G. W. Wint, and D. J. Rogers (2008), Global data
939   for ecology and epidemiology: a novel algorithm for temporal Fourier processing MODIS data, PloS one, 3(1),
940   e1408.

941 Seneviratne, S. I., T. Corti, E. L. Davin, M. Hirschi, E. B. Jaeger, I. Lehner, B. Orlowsky, and A. J. Teuling (2010),
942   Investigating soil moisture-climate interactions in a changing climate: A review, Earth Science Reviews, 99(3),
943   125-161.

944 Srivastava, P. K., D. Han, M. A. R. Ramirez, and T. Islam (2013), Appraisal of SMOS soil moisture at a catchment
945   scale in a temperate maritime climate, Journal of Hydrology, 498, 292-304.

946 Su, C. H., D. Ryu, A. W. Western, and W. Wagner (2013a), De-noising of passive and active microwave satellite soil
947   moisture time series, Geophysical Research Letters, 40(14), 3624-3630.

948 Su, C. H., D. Ryu, R. I. Young, A. W. Western, and W. Wagner (2013b), Inter-comparison of microwave satellite soil
949   moisture retrievals over the Murrumbidgee Basin, southeast Australia, Remote Sensing of Environment, 134, 1-
950   11.

951 Su, C. H., S. Y. Narsey, A. Gruber, A. Xaver, D. Chung, D. Ryu, and W. Wagner (2015), Evaluation of post-retrieval
952   de-noising of active and passive microwave satellite soil moisture, Remote Sensing of Environment, 163, 127-
953   139.

954 Van der Schalie, R., R. Parinussa, L. J. Renzullo, A. Van Dijk, C.-H. Su, and R. A. de Jeu (2015), SMOS soil moisture
955   retrievals using the land parameter retrieval model: Evaluation over the Murrumbidgee Catchment, southeast
956   Australia, Remote Sensing of Environment, 163, 70-79.

957 Van der Schalie, R., Y. Kerr, J. Wigneron, N. Rodríguez-Fernández, A. Al-Yaari, and R. de Jeu (2016), Global SMOS
958   soil moisture retrievals from the land parameter retrieval model, International Journal of Applied Earth
959   Observation and Geoinformation, 45, 125-134.

960 Wagner, W., G. Blöschl, P. Pampaloni, J. C. Calvet, B. Bizzarri, J. P. Wigneron, and Y. Kerr (2007a), Operational
961   readiness of microwave remote sensing of soil moisture for hydrologic applications, Hydrology Research, 38(1),
962   1-20.

963 Wagner, W., V. Naeimi, K. Scipal, R. de Jeu, and J. Martínez-Fernández (2007b), Soil moisture from operational
964   meteorological satellites, Hydrogeology Journal, 15(1), 121-131.

965 Walker, J. P., and P. R. Houser (2004), Requirements of a global near-surface soil moisture satellite mission: accuracy,
966   repeat time, and spatial resolution, Advances in Water Resources, 27(8), 785-801.

967 Wang, G., D. Garcia, Y. Liu, R. de Jeu, and A. J. Dolman (2012), A three-dimensional gap filling method for large
968   geophysical datasets: Application to global satellite soil moisture observations, Environmental Modelling and
969   Software, 30, 139-142.

970 Wang, J., and B. Choudhury (1981), Remote sensing of soil moisture content, over bare field at 1.4 GHz frequency,
971   Journal of Geophysical Research: Oceans, 86(C6), 5277-5282.

972 Wang, J. R., and T. J. Schmugge (1980), An empirical model for the complex dielectric permittivity of soils as a
973   function of water content, IEEE Transactions on Geoscience and Remote Sensing, 4(GE-18), 288-295.

974 Weng, F. (2010), Observations and simulations of microwave land emissivity. European Centre for Medium-Range
975   Weather Forecasts — Joint Center for Satellite Data Assimilation (ECMWF—JCSDA) Workshop, June 15-17,
976   Reading, UK.

977 Wu, W., and R. E. Dickinson (2004), Time Scales of Layered Soil Moisture Memory in the Context of Land-
978   Atmosphere Interaction, Journal of Climate, 17(14), 2752-2764.